Di-jet production in photon-photon collisions at $\sqrt{s_{\mathrm{ee}}}$ from 189 to 209 GeV

The OPAL Collaboration

G. Abbiendi[2], C. Ainsley[5], P.F. Åkesson[3], G. Alexander[22], J. Allison[16], P. Amaral[9], G. Anagnostou[1], K.J. Anderson[9], S. Arcelli[2], S. Asai[23], D. Axen[27], G. Azuelos[18,a], I. Bailey[26], E. Barberio[8,p], R.J. Barlow[16], R.J. Batley[5], P. Bechtle[25], T. Behnke[25], K.W. Bell[20], P.J. Bell[1], G. Bella[22], A. Bellerive[6], G. Benelli[4], S. Bethke[32], O. Biebel[31], I.J. Bloodworth[1], O. Boeriu[10], P. Bock[11], D. Bonacorsi[2], M. Boutemeur[31], S. Braibant[8], L. Brigliadori[2], R.M. Brown[20], K. Buesser[25], H.J. Burckhart[8], S. Campana[4], R.K. Carnegie[6], B. Caron[28], A.A. Carter[13], J.R. Carter[5], C.Y. Chang[17], D.G. Charlton[1,b], A. Csilling[8,g], M. Cuffiani[2], S. Dado[21], S. Dallison[16], A. De Roeck[8], E.A. De Wolf[8,s], K. Desch[25], B. Dienes[30], M. Donkers[6], J. Dubbert[31], E. Duchovni[24], G. Duckeck[31], I.P. Duerdoth[16], E. Elfgren[18], E. Etzion[22], F. Fabbri[2], L. Feld[10], P. Ferrari[8], F. Fiedler[31], I. Fleck[10], M. Ford[5], A. Frey[8], A. Fürtjes[8], P. Gagnon[12], J.W. Gary[4], G. Gaycken[25], C. Geich-Gimbel[3], G. Giacomelli[2], P. Giacomelli[2], M. Giunta[4], J. Goldberg[21], E. Gross[24], J. Grunhaus[22], M. Gruwé[8], P.O. Günther[3], A. Gupta[9], C. Hajdu[29], M. Hamann[25], G.G. Hanson[4], K. Harder[25], A. Harel[21], M. Harin-Dirac[4], M. Hauschild[8], J. Hauschildt[25], C.M. Hawkes[1], R. Hawkings[8], R.J. Hemingway[6], C. Hensel[25], G. Herten[10], R.D. Heuer[25], J.C. Hill[5], K. Hoffman[9], R.J. Homer[1], D. Horváth[29,c], R. Howard[27], P. Igo-Kemenes[11], K. Ishii[23], H. Jeremie[18], P. Jovanovic[1], T.R. Junk[6], N. Kanaya[26], J. Kanzaki[23], G. Karapetian[18], D. Karlen[6], V. Kartvelishvili[16], K. Kawagoe[23], T. Kawamoto[23], R.K. Keeler[26], R.G. Kellogg[17], B.W. Kennedy[20], D.H. Kim[19], K. Klein[11,t], A. Klier[24], S. Kluth[32], T. Kobayashi[23], M. Kobel[3], S. Komamiya[23], L. Kormos[26], T. Krämer[25], T. Kress[4], P. Krieger[6,l], J. von Krogh[11], D. Krop[12], K. Kruger[8], T. Kuhl[25], M. Kupper[24], G.D. Lafferty[16], H. Landsman[21], D. Lanske[14], J.G. Layter[4], A. Leins[31], D. Lellouch[24], J. Letts[o], L. Levinson[24], J. Lillich[10], S.L. Lloyd[13], F.K. Loebinger[16], J. Lu[27], J. Ludwig[10], A. Macpherson[28,i], W. Mader[3], S. Marcellini[2], T.E. Marchant[16], A.J. Martin[13], J.P. Martin[18], G. Masetti[2], T. Mashimo[23], P. Mättig[m], W.J. McDonald[28], J. McKenna[27], T.J. McMahon[1], R.A. McPherson[26], F. Meijers[8], P. Mendez-Lorenzo[31], W. Menges[25], F.S. Merritt[9], H. Mes[6,a], A. Michelini[2], S. Mihara[23], G. Mikenberg[24], D.J. Miller[15], S. Moed[21], W. Mohr[10], T. Mori[23], A. Mutter[10], K. Nagai[13], I. Nakamura[23], H.A. Neal[33], R. Nisius[32], S.W. O'Neale[1], A. Oh[8], A. Okpara[11], M.J. Oreglia[9], S. Orito[23], C. Pahl[32], G. Pásztor[4,g], J.R. Pater[16], G.N. Patrick[20], J.E. Pilcher[9], J. Pinfold[28], D.E. Plane[8], B. Poli[2], J. Polok[8], O. Pooth[14], M. Przybycień[8,n], A. Quadt[3], K. Rabbertz[8,r], C. Rembser[8], P. Renkel[24], H. Rick[4], J.M. Roney[26], S. Rosati[3], Y. Rozen[21], K. Runge[10], K. Sachs[6], T. Saeki[23], O. Sahr[31], E.K.G. Sarkisyan[8,j], A.D. Schaile[31], O. Schaile[31], P. Scharff-Hansen[8], J. Schieck[32], T. Schörner-Sadenius[8], M. Schröder[8], M. Schumacher[3], C. Schwick[8], W.G. Scott[20], R. Seuster[14,f], T.G. Shears[8,h], B.C. Shen[4], P. Sherwood[15], G. Siroli[2], A. Skuja[17], A.M. Smith[8], R. Sobie[26], S. Söldner-Rembold[10,d], F. Spano[9], A. Stahl[3], K. Stephens[16], D. Strom[19], R. Ströhmer[31], S. Tarem[21], M. Tasevsky[8], R.J. Taylor[15], R. Teuscher[9], M.A. Thomson[5], E. Torrence[19], D. Toya[23], P. Tran[4], T. Trefzger[31], A. Tricoli[2], I. Trigger[8], Z. Trócsányi[30,e], E. Tsur[22], M.F. Turner-Watson[1], I. Ueda[23], B. Ujvári[30,e], B. Vachon[26], C.F. Vollmer[31], P. Vannerem[10], M. Verzocchi[17], H. Voss[8,q], J. Vossebeld[8,h], D. Waller[6], C.P. Ward[5], D.R. Ward[5], P.M. Watkins[1], A.T. Watson[1], N.K. Watson[1], P.S. Wells[8], T. Wengler[8], N. Wermes[3], D. Wetterling[11] G.W. Wilson[16,k], J.A. Wilson[1], G. Wolf[24], T.R. Wyatt[16], S. Yamashita[23], D. Zer-Zion[4], L. Zivkovic[24]

[1] School of Physics and Astronomy, University of Birmingham, Birmingham B15 2TT, UK
[2] Dipartimento di Fisica dell' Università di Bologna and INFN, 40126 Bologna, Italy
[3] Physikalisches Institut, Universität Bonn, 53115 Bonn, Germany
[4] Department of Physics, University of California, Riverside CA 92521, USA
[5] Cavendish Laboratory, Cambridge CB3 0HE, UK
[6] Ottawa-Carleton Institute for Physics, Department of Physics, Carleton University, Ottawa, Ontario K1S 5B6, Canada
[8] CERN, European Organisation for Nuclear Research, 1211 Geneva 23, Switzerland
[9] Enrico Fermi Institute and Department of Physics, University of Chicago, Chicago IL 60637, USA
[10] Fakultät für Physik, Albert-Ludwigs-Universität Freiburg, 79104 Freiburg, Germany
[11] Physikalisches Institut, Universität Heidelberg, 69120 Heidelberg, Germany
[12] Indiana University, Department of Physics, Bloomington IN 47405, USA
[13] Queen Mary and Westfield College, University of London, London E1 4NS, UK
[14] Technische Hochschule Aachen, III Physikalisches Institut, Sommerfeldstrasse 26-28, 52056 Aachen, Germany
[15] University College London, London WC1E 6BT, UK
[16] Department of Physics, Schuster Laboratory, The University, Manchester M13 9PL, UK

[17] Department of Physics, University of Maryland, College Park, MD 20742, USA

[18] Laboratoire de Physique Nucléaire, Université de Montréal, Montréal, Québec H3C 3J7, Canada

[19] University of Oregon, Department of Physics, Eugene OR 97403, USA

[20] CLRC Rutherford Appleton Laboratory, Chilton, Didcot, Oxfordshire OX11 0QX, UK

[21] Department of Physics, Technion-Israel Institute of Technology, Haifa 32000, Israel

[22] Department of Physics and Astronomy, Tel Aviv University, Tel Aviv 69978, Israel

[23] International Centre for Elementary Particle Physics and Department of Physics, University of Tokyo, Tokyo 113-0033, and Kobe University, Kobe 657-8501, Japan

[24] Particle Physics Department, Weizmann Institute of Science, Rehovot 76100, Israel

[25] Universität Hamburg/DESY, Institut für Experimentalphysik, Notkestrasse 85, 22607 Hamburg, Germany

[26] University of Victoria, Department of Physics, P O Box 3055, Victoria BC V8W 3P6, Canada

[27] University of British Columbia, Department of Physics, Vancouver BC V6T 1Z1, Canada

[28] University of Alberta, Department of Physics, Edmonton AB T6G 2J1, Canada

[29] Research Institute for Particle and Nuclear Physics, 1525 Budapest, P O Box 49, Hungary

[30] Institute of Nuclear Research, 4001 Debrecen, P O Box 51, Hungary

[31] Ludwig-Maximilians-Universität München, Sektion Physik, Am Coulombwall 1, 85748 Garching, Germany

[32] Max-Planck-Institute für Physik, Föhringer Ring 6, 80805 München, Germany

[33] Yale University, Department of Physics, New Haven, CT 06520, USA

Abstract. Di-jet production is studied in collisions of quasi-real photons at e^+e^- centre-of-mass energies $\sqrt{s_{ee}}$ from 189 to 209 GeV at LEP. The data were collected with the OPAL detector. Jets are reconstructed using an inclusive $k_\perp$-clustering algorithm for all cross-section measurements presented. A cone jet algorithm is used in addition to study the different structure of the jets resulting from either of the algorithms. The inclusive di-jet cross-section is measured as a function of the mean transverse energy $\bar{E}_{\mathrm{T}}^{\mathrm{jet}}$ of the two leading jets, and as a function of the estimated fraction of the photon momentum carried by the parton entering the hard sub-process, x_γ, for different regions of $\bar{E}_{\mathrm{T}}^{\mathrm{jet}}$. Angular distributions in di-jet events are measured and used to demonstrate the dominance of quark and gluon initiated processes in different regions of phase space. Furthermore the inclusive di-jet cross-section as a function of $|\eta^{\mathrm{jet}}|$ and $|\Delta\eta^{\mathrm{jet}}|$ is presented, where η^{jet} is the jet pseudo-rapidity. Different regions of the x_γ^+-x_γ^--space are explored to study and control the influence of an underlying event. The results are compared to next-to-leading order perturbative QCD calculations and to the predictions of the leading order Monte Carlo generator PYTHIA.

Correspondence to: [a] and at TRIUMF, Vancouver, Canada V6T 2A3

[b] and Royal Society University Research Fellow

[c] and Institute of Nuclear Research, Debrecen, Hungary

[d] and Heisenberg Fellow

[e] and Department of Experimental Physics, Lajos Kossuth University, Debrecen, Hungary

[f] and MPI München

[g] and Research Institute for Particle and Nuclear Physics, Budapest, Hungary

[h] now at University of Liverpool, Dept of Physics, Liverpool L69 3BX, U.K.

[i] and CERN, EP Div, 1211 Geneva 23

[j] now at University of Nijmegen, HEFIN, NL-6525 ED Nijmegen,The Netherlands, on NWO/NATO Fellowship B 64-29

[k] now at University of Kansas, Dept of Physics and Astronomy, Lawrence, KS 66045, USA

[l] now at University of Toronto, Dept of Physics, Toronto, Canada

[m] current address Bergische Universität, Wuppertal, Germany

[n] and University of Mining and Metallurgy, Cracow, Poland

[o] now at University of California, San Diego, USA

[p] now at Physics Dept Southern Methodist University, Dallas, TX 75275, USA

[q] now at IPHE Université de Lausanne, 1015 Lausanne, Switzerland

[r] now at IEKP Universität Karlsruhe, Germany

[s] now at Universitaire Instelling Antwerpen, Physics Department, 2610 Antwerpen, Belgium [t] now at RWTH Aachen, Germany

1 Introduction

We have studied the production of di-jets in the collisions of two quasi-real photons at an e^+e^- centre-of-mass energy $\sqrt{s_{ee}}$ from 189 to 209 GeV, with a total integrated luminosity of 593 pb^{-1} collected by the OPAL detector at LEP. Di-jet events are of particular interest, as the two jets can be used to estimate the fraction of the photon momentum participating in the hard interaction, which is a sensitive probe of the structure of the photon. The transverse energy of the jets provides a hard scale that allows such processes to be calculated in perturbative QCD. Fixed order calculations at next-to-leading order (NLO) in the strong coupling constant α_s for di-jet production are available and are compared to the data, providing tests of the theory. Leading order Monte Carlo (MC) generators are used to estimate the importance of soft processes not included in the NLO calculation.

Inclusive jet cross-sections in photon-photon collisions have previously been measured at $\sqrt{s_{ee}} = 58$ GeV at TRISTAN [1, 2] and at $\sqrt{s_{ee}}$ from 130 to 172 GeV at LEP [3,4]. This paper extends the latter analysis to higher e^+e^- centre-of-mass energies, and provides an approximately thirty-fold increase in integrated luminosity. The $k_\perp$-clustering algorithm [5] is used as opposed to the cone algorithm [6] in [3,4] for the measurement of the differential cross-sections, because of the advantages of this algorithm in comparing to theoretical calculations [7]. The cone jet algorithm is used to demonstrate the different structure of the cone jets compared to jets defined by the $k_\perp$-clustering algorithm. The large amount of data allows us to measure the cross-section for di-jet production in photon-photon interactions as a function of the mean transverse jet energy $\bar{E}_T^{jet}$, the jet pseudo-rapidity $|\eta^{jet}|$ and the absolute difference in pseudo-rapidity $|\Delta\eta^{jet}|$ of the jets, with $\eta^{jet} = -\ln\tan(\theta^{jet}/2)$ [1]. For the first time, the differential cross-section is also measured as a function of the estimated fraction of the photon momentum carried by the parton entering the hard sub-process, x_γ, with full unfolding for detector effects. Angular distributions in di-jet events are measured and used to demonstrate the dominance of quark and gluon initiated processes in different regions of phase space.

At e^+e^- colliders the photons are emitted by the beam electrons[2]. Most of these photons carry only a small negative four-momentum squared, Q^2, and can be considered quasi-real ($Q^2 \approx 0$). The electrons are hence scattered with very small polar angles and are not detected. Events where one or both scattered electrons are detected are not considered in the present analysis. Three processes contribute to di-jet production in photon-photon collisions: the direct process where two bare photons interact, the single-resolved process where a bare photon picks out a parton (quark or gluon) of the other photon, and the double-resolved process where partons of both photons interact [8]. This separation is only unambiguous at leading order. At higher orders it becomes dependent on the process scales.

2 The OPAL detector

A detailed description of the OPAL detector can be found in [9]. Only the main features relevant to the present analysis will be given here.

The central tracking system is located inside a solenoidal magnet which provides a uniform axial magnetic field of 0.435 T along the beam axis. The magnet is surrounded in the barrel region ($|\cos\theta| < 0.82$) by a lead glass electromagnetic calorimeter (ECAL) and a hadronic sampling calorimeter (HCAL). Outside the HCAL, the detector is surrounded by muon chambers. There are similar

layers of detectors in the endcaps ($0.82 < |\cos\theta| < 0.98$). The small angle region from 47 to 140 mrad around the beam pipe on both sides of the interaction point is covered by the forward calorimeters (FD) and the region from 33 to 59 mrad by the silicon tungsten luminometers (SW).

Starting with the innermost components, the tracking system consists of a high precision silicon micro-vertex detector, a vertex drift chamber, a large volume jet chamber with 159 layers of axial anode wires and a set of z chambers measuring the track coordinates along the beam direction.

The barrel and endcap sections of the ECAL are both constructed from lead glass blocks with a depth of 24.6 radiation lengths in the barrel region and more than 22 radiation lengths in the endcaps. The HCAL consists of streamer tubes and thin multiwire chambers instrumenting the gaps in the iron yoke of the magnet, which provides the absorber material of 4 or more interaction lengths.

The FD consists of two cylindrical lead-scintillator calorimeters with a depth of 24 radiation lengths divided azimuthally into 16 segments. The SW detectors consist of 19 layers of silicon detectors and 18 layers of tungsten, corresponding to a total of 22 radiation lengths.

3 Monte Carlo simulation

The MC generators PYTHIA 5.722 [10,11] and PHOJET 1.10 [12] are used to study detector effects. PYTHIA is based on leading order (LO) QCD matrix elements for massless quarks with added parton showers and hadronisation. PHOJET also simulates hard interactions through perturbative QCD in LO, but includes soft interactions through Regge phenomenology before the partons are hadronised. The probability of finding a parton in the photon is taken from parametrisations of the parton distribution functions. The default choices of SaS 1D [13] for PYTHIA and LO GRV [14] for PHOJET are taken for the samples used to study detector effects.

An increased flow of transverse energy, E_T, apparently not directly related to the hard subprocess has been observed in photon-hadron scattering [15], and has been labelled the underlying event. Both PHOJET and PYTHIA include a model of multiple parton interactions (MIA) to simulate such effects. In PYTHIA the amount of MIA added to the event is controlled by a lower cutoff parameter p_t^{mi}, which describes the transverse momentum of the parton involved. Following the studies carried out in [3,4], p_t^{mi} is set to 1.4 GeV for the SaS 1D parton densities. In PHOJET the default setting for MIA is used.

Three non-signal processes are important: hadronic decays of the Z^0, where initial state photon radiation has reduced the centre-of-mass energy of the hadronic final state to be close to the Z^0 mass, $\gamma\gamma \to \tau\tau$ reactions, and photon-photon collisions where one of the photons is virtual ($\gamma^\star\gamma$) but the scattered electron is not detected. The hadronic Z^0 decays are simulated using PYTHIA 6.1. The pair-production of τ-leptons in photon-photon collisions is simulated using BDK [16]. Deep-inelastic electron-photon scattering events are studied with the HERWIG 5.9 [17] generator.
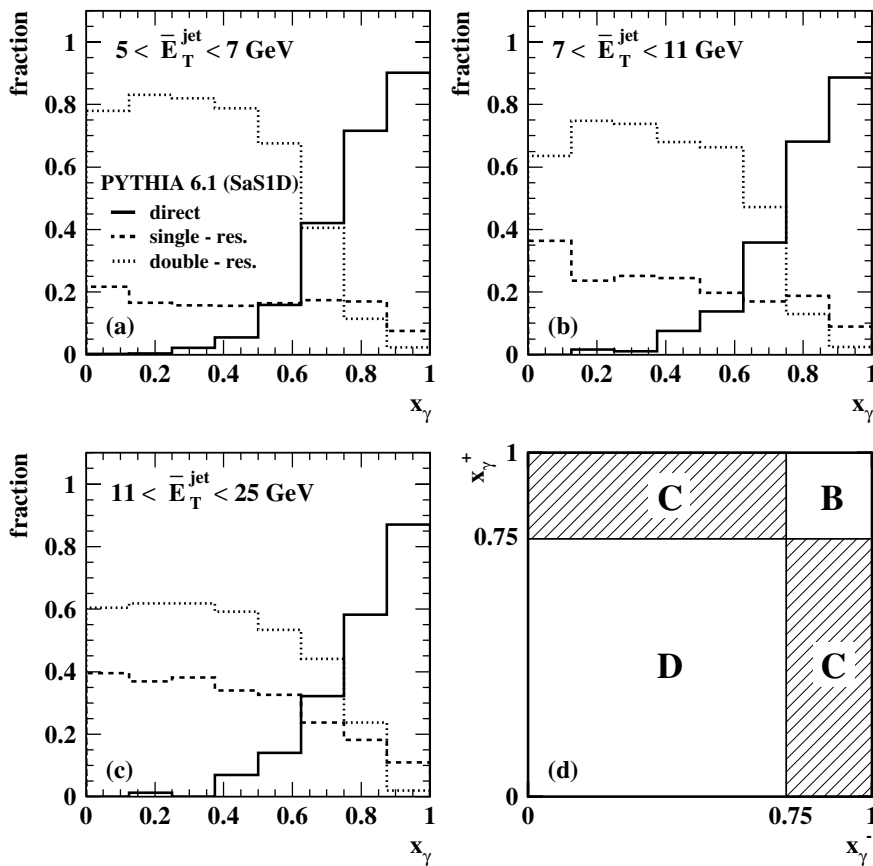
---

[1] The coordinate system of OPAL has the z axis along the electron beam direction, the y axis pointing upwards and x towards the center of the LEP ring. The polar angle θ and the azimuthal angle ϕ are defined relative to the $+z$-axis and $+x$-axis, respectively

[2] Positrons are also referred to as electrons

Fig. 1. a–c. The relative contribution of direct, single-resolved, and double-resolved processes according to PYTHIA at the hadron level for the cross-sections as a function of x_γ for the full x_γ^+-x_γ^--range (see Sect. 4). In **d** the regions in x_γ^+-x_γ^--space used in addition to the full x_γ^+-x_γ^--range (referred to as (A)) are illustrated: (B) both x_γ^+ and x_γ^- larger than 0.75 ($x_\gamma^\pm > 0.75$), (C) either x_γ^+ or x_γ^- smaller than 0.75 (x_γ^+ or $x_\gamma^- < 0.75$), (D) both x_γ^+ and x_γ^- smaller than 0.75 ($x_\gamma^\pm < 0.75$)

All signal and background MC samples were generated with the full simulation of the OPAL detector [18]. They are analysed using the same reconstruction algorithms as are applied to the data.

Although PYTHIA 5.722 is used to correct for detector effects to make use of the large number of signal events with full detector simulation available in OPAL, we have used PYTHIA 6.121 for our study of hadronisation effects in Sect. 9 and for comparisons with the data in Sect. 10. In both cases it is desirable to use the latest version of the generator and no simulation of the OPAL detector is required. Since PHOJET uses the same string hadronisation model as PYTHIA, HERWIG 6.1, which uses cluster fragmentation, was used as an alternative model to estimate the hadronisation corrections in Sect. 9.

4 Definition of di-jet observables

All cross-section measurements use jets reconstructed with the inclusive $k_\perp$-clustering algorithm as proposed in [5] with $R_0 = 1$. In addition, a cone jet algorithm [6] with a cone size of 1.0 in η-ϕ-space is employed to study the dependence of the jet structure on the algorithm used. A di-jet event is defined as an event with at least two jets

fulfilling the requirements detailed below. In events with more than two jets, only the two jets with the highest E_T^{jet} values are taken.

The primary intentions of this analysis are to study the ability of QCD theory to describe jet production in photon-photon collisions, and to explore the photon structure revealed in these hadronic interactions. The most advanced theoretical predictions to date are provided by fixed order perturbative calculations up to NLO for the production of di-jets. These calculations need as input a scale that is in principle arbitrary, but commonly set to a value related to the hardness of the interaction. Possible choices for di-jet production are for example the mean transverse energy $\bar{E}_T^{jet}$ or the maximum E_T^{jet} of the di-jet system.

The separation of quasi-real and virtual photons is somewhat arbitrary and therefore needs to be defined. For this analysis we choose values of $Q^2 < 4.5\,\text{GeV}^2$ to define quasi-real photons. It is the same value as used in previous analyses [3,4], motivated by the acceptance of the low angle calorimeters. The median Q^2 resulting from this definition cannot be determined with the data since the scattered electrons are not tagged. For the kinematic range of this analysis both PHOJET and PYTHIA predict the median Q^2 to be of the order $10^{-4}\,\text{GeV}^2$.

4.1 Properties of di-jet events

In LO QCD, neglecting multiple parton interactions, two hard parton jets are produced in $\gamma\gamma$ interactions. In single- or double-resolved interactions, these jets are expected to be accompanied by one or two remnant jets. A pair of variables, x_γ^+ and x_γ^-, can be defined [19] that estimate the fraction of the photon's momentum participating in the hard scattering:

$$x_\gamma^+ \equiv \frac{\sum\limits_{\mathrm{jets}=1,2} \left(E^{\mathrm{jet}} + p_z^{\mathrm{jet}}\right)}{\sum\limits_{\mathrm{hfs}} \left(E + p_z\right)} \quad \text{and}$$

$$x_\gamma^- \equiv \frac{\sum\limits_{\mathrm{jets}=1,2} \left(E^{\mathrm{jet}} - p_z^{\mathrm{jet}}\right)}{\sum\limits_{\mathrm{hfs}} \left(E - p_z\right)}, \tag{1}$$

where p_z is the momentum component along the z axis of the detector and E is the energy of the jets or objects of the hadronic final state (hfs). In LO, for direct events, all energy of the event is contained in two jets, i.e., $x_\gamma^+ = 1$ and $x_\gamma^- = 1$, whereas for single-resolved or double-resolved events one or both values are smaller than 1. The di-jet differential cross-section as a function of x_γ is therefore particularly well suited to study the structure of the photon, since it separates predominantly direct events at high x_γ ($x_\gamma > 0.75$) from predominantly resolved events at low x_γ ($x_\gamma < 0.75$). The fraction of direct, single-resolved and double-resolved events as a function of x_γ predicted by PYTHIA is shown in Fig. 1a–c. The dominance of resolved events for $x_\gamma < 0.75$ is clearly visible. In these distributions and in the definitions below, x_γ indicates that each event enters the distribution twice, at the value of x_γ^+ and the value of x_γ^-.

Due to the different nature of the underlying partonic process one expects different distributions of the angle Θ^* between the jet axis and the axis of the incoming partons or direct photons in the di-jet centre-of-mass frame. The leading order direct process $\gamma\gamma \to q\bar{q}$ proceeds via the t-channel exchange of a spin-$\frac{1}{2}$ quark, which leads to an angular dependence $\propto \left(1 - \cos^2\Theta^*\right)^{-1}$. In double resolved processes the sum of all matrix elements, including a large contribution from spin-1 gluon exchange, leads to an approximate angular dependence $\propto \left(1 - |\cos\Theta^*|\right)^{-2}$ [20]. The contribution of the different processes to all resolved events depends on the parton distribution functions of the photon. An estimator of the angle Θ^* can be formed from the pseudo-rapidities of the two jets as

$$\cos\Theta^* = \tanh\left(\frac{\eta_1^{\mathrm{jet}} - \eta_2^{\mathrm{jet}}}{2}\right), \tag{2}$$

where it is assumed that the jets are collinear in ϕ and have equal transverse energy. Only $|\cos\Theta^*|$ can be measured, as the ordering of the jets in the detector is arbitrary. To obtain an unbiased distribution of $|\cos\Theta^*|$ the measurement needs to be restricted to the region where the di-jet invariant mass $M_{\mathrm{jj}} = 2\bar{E}_{\mathrm{T}}^{\mathrm{jet}}/\sqrt{1 - |\cos\Theta^*|^2}$ is not influenced by the cuts on $E_{\mathrm{T}}^{\mathrm{jet}}$ [4]. In the present analysis a cut of $M_{\mathrm{jj}} > 15\,\mathrm{GeV}$ ensures that the $|\cos\Theta^*|$ distribution is not biased by the restrictions on $E_{\mathrm{T}}^{\mathrm{jet}}$ for the range $|\cos\Theta^*| < 0.8$ and $|\bar{\eta}^{\mathrm{jet}}| = |\left(\eta_1^{\mathrm{jet}} + \eta_2^{\mathrm{jet}}\right)/2| < 1$ confines the measurement to the region where the detector resolution on $|\cos\Theta^*|$ is good.

4.2 Differential di-jet cross-sections

The following differential cross-sections are measured, where the labels 1 and 2 refer to the two jets with highest $E_{\mathrm{T}}^{\mathrm{jet}}$ in the event, defined by the $k_\perp$ algorithm:

$$\frac{\mathrm{d}\sigma_{\mathrm{dijet}}}{\mathrm{d}\bar{E}_{\mathrm{T}}^{\mathrm{jet}}} \quad \text{with} \quad \bar{E}_{\mathrm{T}}^{\mathrm{jet}} \equiv \frac{E_{\mathrm{T},1}^{\mathrm{jet}} + E_{\mathrm{T},2}^{\mathrm{jet}}}{2}$$

$$\text{and} \quad \bar{E}_{\mathrm{T}}^{\mathrm{jet}} > 5\,\mathrm{GeV}, \tag{3}$$

$$\frac{\mathrm{d}\sigma_{\mathrm{dijet}}}{\mathrm{d}x_\gamma} \quad \text{in 3 bins of}$$

$$\bar{E}_{\mathrm{T}}^{\mathrm{jet}} \; [5\text{–}7\text{–}11\text{–}25]\,\mathrm{GeV}, \tag{4}$$

$$\frac{\mathrm{d}\sigma_{\mathrm{dijet}}}{\mathrm{d}\log_{10}(x_\gamma)} \quad \text{for} \quad 5\,\mathrm{GeV} < \bar{E}_{\mathrm{T}}^{\mathrm{jet}} < 7\,\mathrm{GeV}, \tag{5}$$

$$\frac{\mathrm{d}\sigma_{\mathrm{dijet}}}{\mathrm{d}|\eta_{\mathrm{cntr}}^{\mathrm{jet}}|}, \frac{\mathrm{d}\sigma_{\mathrm{dijet}}}{\mathrm{d}|\eta_{\mathrm{fwd}}^{\mathrm{jet}}|}, \frac{\mathrm{d}\sigma_{\mathrm{dijet}}}{\mathrm{d}|\Delta\eta^{\mathrm{jet}}|} \quad \text{for} \quad \bar{E}_{\mathrm{T}}^{\mathrm{jet}} > 5\,\mathrm{GeV}, \tag{6}$$

$$\frac{\mathrm{d}\sigma_{\mathrm{dijet}}}{\mathrm{d}|\cos\Theta^*|} \quad \text{for} \quad \bar{E}_{\mathrm{T}}^{\mathrm{jet}} > 5\,\mathrm{GeV}, \; |\bar{\eta}^{\mathrm{jet}}| < 1,$$

$$M_{\mathrm{jj}} > 15\,\mathrm{GeV} \tag{7}$$

with in all cases

$$|\eta_{1,2}^{\mathrm{jet}}| < 2 \quad \text{and} \quad \frac{|E_{\mathrm{T},1}^{\mathrm{jet}} - E_{\mathrm{T},2}^{\mathrm{jet}}|}{E_{\mathrm{T},1}^{\mathrm{jet}} + E_{\mathrm{T},2}^{\mathrm{jet}}} < \frac{1}{4}. \tag{8}$$

Here, $|\eta_{\mathrm{cntr}}^{\mathrm{jet}}|$ and $|\eta_{\mathrm{fwd}}^{\mathrm{jet}}|$ denote the jet with the smaller and larger value of $|\eta^{\mathrm{jet}}|$ respectively, and $|\Delta\eta^{\mathrm{jet}}|$ is defined to be the absolute distance in pseudo-rapidity between the two leading jets.

The combination of the second condition in (8) with the minimum $\bar{E}_{\mathrm{T}}^{\mathrm{jet}}$ requirement defines asymmetric $E_{\mathrm{T}}^{\mathrm{jet}}$ thresholds for the two jets of the di-jet system, which is important in comparisons to NLO QCD calculations [21]. This method of defining asymmetric thresholds has previously been used in [22].

Four regions in x_γ^+-x_γ^--space are considered (see Fig. 1d): (A) the complete x_γ^+-x_γ^--space (full $x_\gamma^\pm$ range), (B) both x_γ^+ and x_γ^- larger than 0.75 ($x_\gamma^\pm > 0.75$), (C) either x_γ^+ or
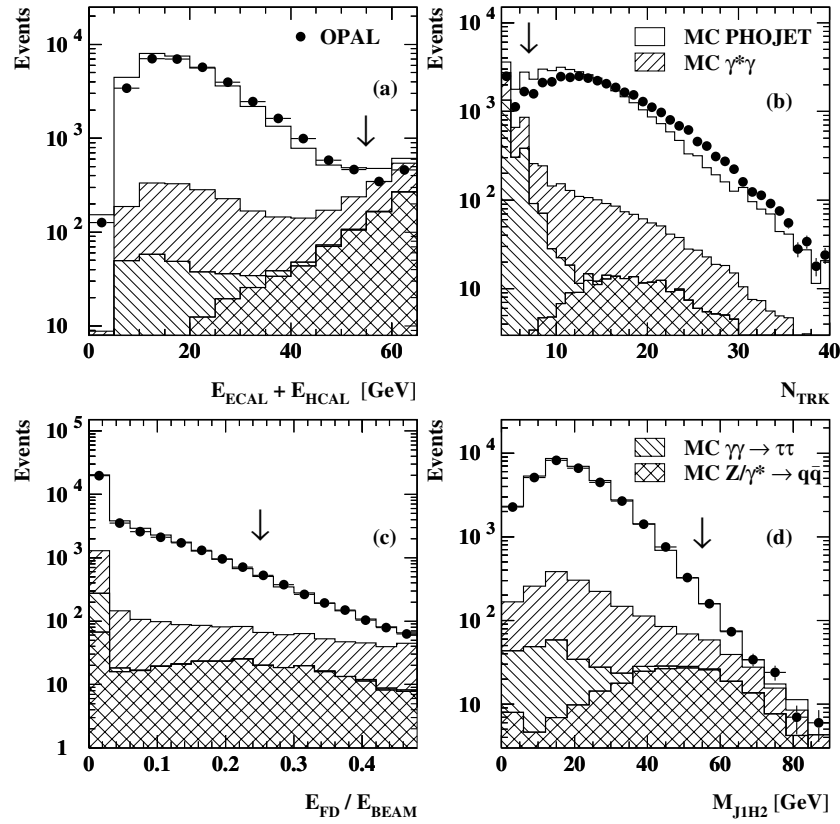
Fig. 2a–d. Comparison of event quantities for uncorrected data with the simulation for the di-jet sample including contributions from background processes. **a** shows the sum of energy measured in the electromagnetic and hadronic calorimeter, **b** the number of tracks in the event, **c** is the sum of energy in the FD detector scaled by the beam energy, and **d** the invariant mass of the jet with the highest E_T^{jet} in the event and the four-vector calculated from all objects in the opposite hemisphere as seen from this jet. The statistical error is shown where larger than the marker size. The label $\gamma^\star\gamma$ stands for simulated photon-photon collision events in which one of the photons has a virtuality larger than $4.5\,\text{GeV}^2$ as discussed in Sect. 4. The arrows indicate the cut value applied to the quantity shown

x_γ^- smaller than 0.75 (x_γ^+ or $x_\gamma^- < 0.75$), (D) both x_γ^+ and x_γ^- smaller than 0.75 ($x_\gamma^\pm < 0.75$).

The cross-sections (3), (4) and (5) are measured in regions (A), (C) and (D). For the cross-sections in (6) regions (C) and (D) are considered. The cross-section as a function of $|\cos\Theta^*|$ in (7) is measured in regions (B) and (D).

4.3 Jet structure in di-jet events

The internal structure of jets is studied using the jet shape, which is defined as the fractional transverse jet energy contained in a subcone of radius r concentric with the jet axis, averaged over all jets of the event sample:

$$\psi(r) \equiv \frac{1}{N_{\text{jets}}} \sum_{\text{jets}} \frac{E_T^{\text{jet}}(r)}{E_T^{\text{jet}}\ (r{=}1.0)}$$

$$\text{with} \quad r = \sqrt{(\Delta\eta)^2 + (\Delta\phi)^2}. \tag{9}$$

N_{jet} is the total number of jets analysed. Both $k_\perp$ and cone jets are analysed in this way. As proposed in [23],

only particles assigned to the jet by the jet finders are considered. Events entering the jet shape distributions are required to have at least two jets with a transverse energy $3\,\text{GeV} < E_T^{\text{jet}} < 20\,\text{GeV}$ and a pseudo-rapidity $|\eta^{\text{jet}}| < 2$. The cone jet algorithm is used in addition to the $k_\perp$-clustering algorithm to demonstrate the different structure of the cone jets with respect to those defined by the $k_\perp$-clustering algorithm.

The jet shape is measured in the two regions of x_γ^+-x_γ^--space, $x_\gamma^\pm < 0.75$ and $x_\gamma^\pm > 0.75$, in four bins of E_T^{jet} with bin boundaries at 3, 6, 9, 12 and 20 GeV and four bins of $|\eta^{\text{jet}}|$ between 0 and 2, each bin 0.5 units wide.

5 Event selection

In this analysis, a sum over all particles in the event or in a jet means a sum over two kinds of objects: tracks and calorimeter clusters, including the FD and SW calorimeters. A track is required to have a minimum transverse momentum of 120 MeV and at least 20 hits in the central jet chamber. The point of closest approach to the origin must have a distance of less than 25 cm in z and a ra-

dial distance of less than 2 cm to the z-axis. Calorimeter clusters have to pass an energy threshold of 100 MeV in the barrel section or 250 MeV in the endcap section for the ECAL, 600 MeV for the barrel and endcap sections of the HCAL, 1 GeV for the FD, and 2 GeV for the SW. An algorithm is applied to avoid double-counting of particle momenta in the central tracking system and their energy deposits in the calorimeters [3]. The measured hadronic final state for each event consists of all objects thus defined.

Di-jet events are preselected using the $k_\perp$ algorithm by requiring at least two jets with $|\eta^{\mathrm{jet}}| < 2$ and a transverse energy $E_{\mathrm{T}}^{\mathrm{jet}} > 3$ GeV. Photon-photon scattering events are selected using the requirements detailed below. The corresponding distributions in Fig. 2 compare the sum of the simulated signal and background processes to the data, uncorrected for detector effects. For each distribution shown, all selection criteria are applied except the one on the quantity plotted. The signal MC generators PHOJET and PYTHIA are found to underestimate the cross-section by about 20% in these comparisons, and are scaled up accordingly. Of all non-signal processes studied, only those listed in Sect. 3 contribute significantly. Comparisons of the rate of di-jet events in photon-photon collisions where one of the photons is virtual (see for example [24]) show that the prediction of the MC generator used is too low by about a factor of two. The prediction of the contribution from $\gamma^\star\gamma$ events has been scaled up accordingly.

All distributions are sufficiently well described by the sum of signal and background contributions. The total contribution of non-signal processes to the selected event sample is about 5% after the following selection criteria have been applied:

- The sum of all energy deposits in the ECAL and HCAL (Fig. 2a) has to be less than 55 GeV to remove background from hadronic Z^0-decays in events with a radiative return to the Z^0-peak.
- The visible invariant mass measured in the ECAL, W_{ECAL}, has to be greater than 3 GeV to suppress low energy events.
- The missing transverse momentum of the event, $P_{\mathrm{T,MISS}}$, calculated from the measured hadronic final state, has to be less than $0.05 \cdot E_{\mathrm{BEAM}}$.
- At least 7 tracks must have been found in the tracking chambers. This cut reduces mostly the contamination from $\gamma\gamma \to \tau\tau$ events. The distribution of the track multiplicity is shown in Fig. 2b. The discrepancy in shape between data and simulation is not present when using PYTHIA instead of PHOJET as signal MC generator, and is addressed in the study of model dependencies in Sect. 8.
- To remove events with scattered electrons in the FD or in the SW calorimeters, the total sum of the energy measured in the FD has to be less than $0.25 \cdot E_{\mathrm{BEAM}}$ and the total sum of the energy measured in the SW calorimeter has to be less than $0.18 \cdot E_{\mathrm{BEAM}}$. These cuts also reduce the contamination from hadronic Z^0-decays with their thrust axis close to the beam direction. The energy sum in the FD calorimeter scaled by the beam energy is shown in Fig. 2c.

- The z position of the primary vertex is required to satisfy $|z| < 5$ cm and the net charge Q of the event calculated from adding the charges of all tracks is required to be $|Q| \le 5$ to reduce background due to beam-gas interactions.
- To remove events originating from interactions between beam electrons and the beam-pipe the radial distance of the primary vertex from the beam axis has to be less than 3 cm.
- To further reject background from hadronic Z^0-decays and from deep-inelastic electron-photon scattering an invariant mass, M_{J1H2}, is calculated from the jet with highest $E_{\mathrm{T}}^{\mathrm{jet}}$ in the event and the four-vector sum of all hadronic final state objects in the hemisphere opposite to the direction defined by this jet. The quantity M_{J1H2} is a simple reconstruction of the Z^0-mass in case of background from hadronic Z^0-decays, and will therefore be larger on average for this type of background than for signal events. Events with $M_{\mathrm{J1H2}} > 55$ GeV are rejected. The distribution of M_{J1H2} is shown in Fig. 2d.

We use data at centre-of-mass energies $\sqrt{s_{ee}}$ from 189 GeV to 209 GeV. For the purpose of this analysis, the difference between the data taken at the various values of $\sqrt{s_{ee}}$ is small and therefore the distributions for all energies have been added. The luminosity weighted average centre-of-mass energy $\sqrt{s_{ee}}$ is approximately 198.5 GeV. The efficiency to trigger di-jet events in the region of phase space considered in this analysis has been shown to be close to 100% [4].

6 Transverse energy flow in di-jet events

NLO QCD calculations do not take into account the possibility of an underlying event which leads to an increased E_{T}-flow and therefore to an increased jet cross-section above a given threshold of $E_{\mathrm{T}}^{\mathrm{jet}}$. In PYTHIA and PHOJET the underlying event is simulated by multiple parton interactions. The contribution from multiple parton interactions is not known a priori, but has to be adjusted to give a good description of the data. In this analysis the size of this contribution is taken from our previous study of di-jet events in [4]. The transverse energy flow from an underlying event is expected to be small compared to the transverse energy of the leading jets, and it is not correlated to the direction of the jet axes. The energy flow outside the jets will therefore be most sensitive to the presence of an underlying event [25]. Additional energy outside the leading jets will shift the x_γ distributions towards lower values.

To study the performance of the MC generators in describing the energy flow several uncorrected distributions are used. The average E_{T}-flow per event is measured with respect to the jet axis as a function of $\Delta\phi$ and $\Delta\hat{\eta}$. The variable $\hat{\eta}$ is equivalent to η, except that it is signed positively if x_γ^+ is greater than or equal x_γ^-, and signed negatively otherwise. The definition of $\hat{\eta}$ ensures that the energy flow associated with the "more resolved" photon, i.e., the
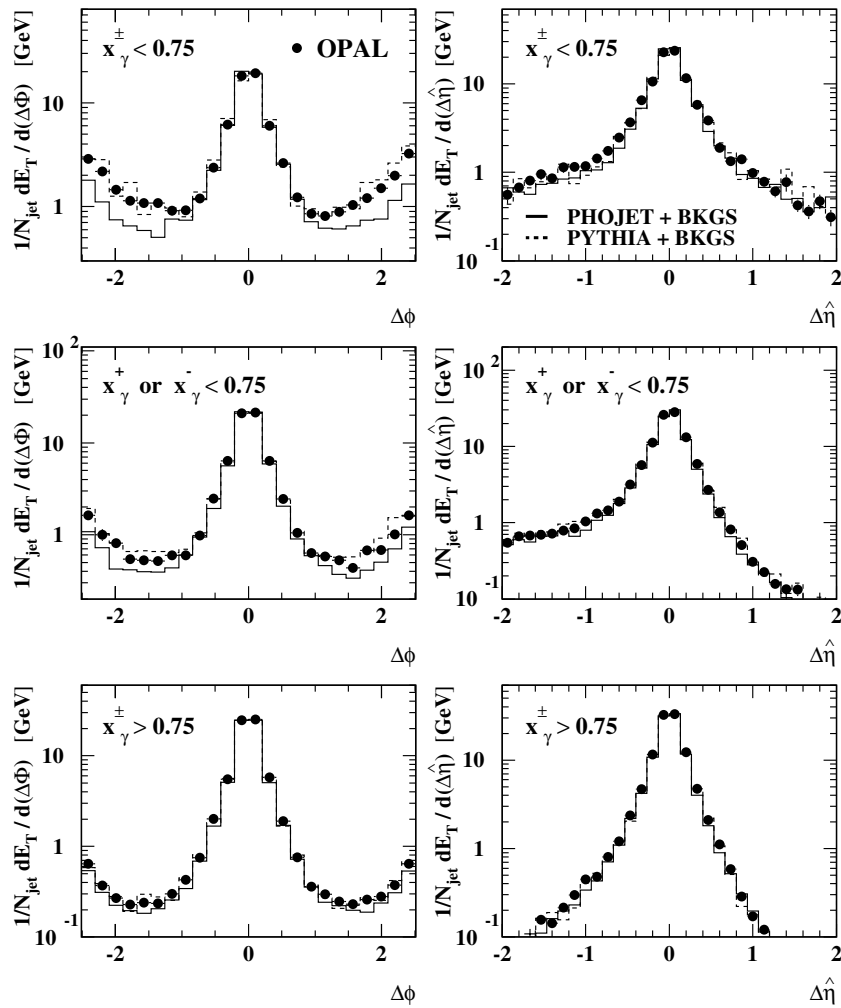
Fig. 3. Jet profiles: The E_T-flow normalised to the number of jets N_{jet} as a function of the distance from the jet axis in ϕ and $\hat{\eta}$. Jets are selected from the range $10 < E_T^{jet} < 25$ GeV. The statistical error is shown where larger than the marker size. The data are compared to a mixture of signal (PHOJET or PYTHIA) and background MC simulation. The background MC simulations used are the same as in Fig. 2

smaller value of x_γ, will always appear on the left hand side of the plots. The profiles in $\Delta\phi$ consider a range of $|\Delta\eta| = 1$ around the jet-axis, while a $|\Delta\phi|$-range of $\pi/2$ around the jet-axis is considered for the profiles in $\Delta\hat{\eta}$. The two leading jets in E_T^{jet} in each event are considered. Another sensitive variable is the energy flow with the leading two jets in the event removed, E^{out}, as a function of $\hat{\eta}$. All objects are excluded inside a cone of radius 1.3 in η-ϕ around the two leading jets.

Multiple parton interactions are important in interactions where the photon is resolved. It is therefore interesting to study separately the three cases of (a) two resolved photons, (b) one resolved photon, or (c) no resolved photon in the interaction. Experimentally these situations can be approximated by choosing events with $x_\gamma^\pm < 0.75$, x_γ^+ or $x_\gamma^- < 0.75$, or $x_\gamma^\pm > 0.75$, i.e. regions (D), (C) and (B) defined in Sect. 4.

Figures 3 and 4 show the jet profiles and the energy flow outside the leading jets. The data are compared to a mixture of signal (PHOJET or PYTHIA) and background MC simulation. The contributions of signal and background are weighted according to their cross-section in each region of phase space. The background MC generators used are the same as in Fig. 2.

For the ϕ-profiles in Fig. 3 it is evident that both PHOJET and PYTHIA are able to describe the data in the region of the high E_T jets around zero. Moving away from the jet axis PHOJET predicts an energy flow which is too low compared to the data, especially for $x_\gamma^\pm < 0.75$. This corresponds to the area where effects from an underlying event are expected to be most prominent. PHOJET improves towards higher x_γ. PYTHIA reproduces the data reasonably well. Such differences between PHOJET and PYTHIA are not evident in the $\hat{\eta}$-profiles. Here in the case of resolved photons the E_T-flow is dominated by the photon remnant(s), and is reasonably well described by both generators. The jets entering Fig. 3 are selected from the range $10 < E_T^{jet} < 25$ GeV. No significant deviation from the behaviour just described is observed when selecting $E_T^{jet} < 10$ GeV.
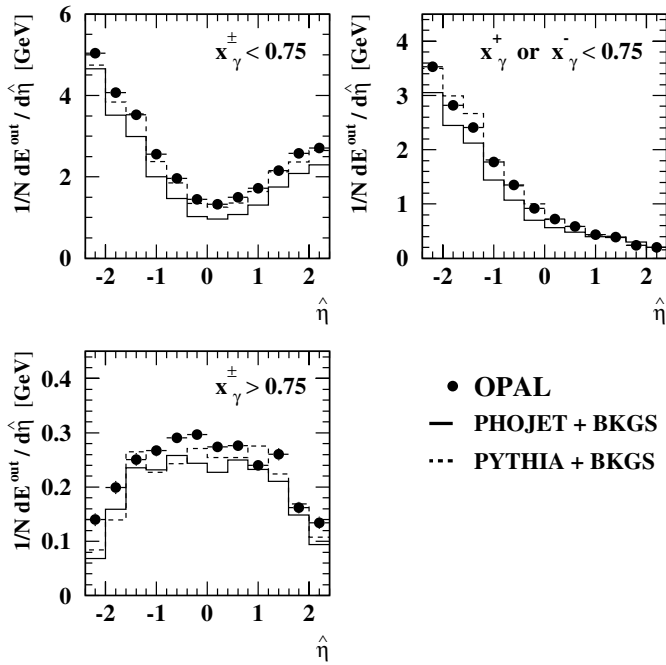
Fig. 4. The energy-flow as a function of $\hat{\eta}$ where the area around the two leading jets in the event has been excluded in a cone of radius 1.3 in η-ϕ-space. The distributions are normalised to the number of di-jet events N. The statistical error is shown where larger than the marker size. The regions in x_γ^+-x_γ^--space considered and the MC simulations used are the same as in Fig. 3

The energy-flow outside the two leading jets is shown in Fig. 4. Again PYTHIA describes the data well, while PHOJET is somewhat low. With both models used to unfold the data as a systematic check, we conclude that the details of the energy flow around the two leading jets are sufficiently well under control and remaining influences are included in the systematic uncertainty of the cross-section and jet shape measurements.

7 Data corrections

An example of the uncorrected distributions as a function of x_γ including the contribution of the remaining background events is shown in Fig. 5. To obtain jet cross-sections which can be compared to theoretical calculations, we use MC simulations to correct for the selection cuts, the resolution effects of the detector and the background from non-signal processes. Backgrounds are first subtracted bin-by-bin from all distributions. For the differential cross-sections as a function of $\bar{E}_T^{\text{jet}}$ and x_γ, sizable migration and resolution effects are to be expected. We therefore apply a matrix unfolding method, as implemented in the GURU program [26], for these distributions. The results are cross checked using a bin-by-bin correction. By definition x_γ can only take values between zero and unity. At either extremity no adjacent bins are available. To avoid instabilities expected from the smoothing procedures in

the unfolding for the first and last bin, the central values for these bins are taken from the bin-by-bin correction method. The $|\cos\Theta^*|$, $|\eta^{\text{jet}}|$ and $|\Delta\eta^{\text{jet}}|$ distributions are corrected bin-by-bin, as only small migrations are expected here. PHOJET is used as the default signal MC generator for the unfolding.

The correction method employed for the jet shapes is a bin-by-bin correction using the MC simulations to correct for detector effects. The contribution of the same background processes as for the cross-section measurements was studied. The influence on the signal was found to be less than 1%. Therefore the subtraction of the background was omitted in this analysis. Both PYTHIA and PHOJET were used to estimate the correction factors to study their model dependence.

8 Systematic uncertainties

The overall systematic uncertainty for each data point measured is determined from the sources listed below added in quadrature. The same sources are considered for the measurement of the differential cross-sections and the jet shapes, with the exception of the background, which has been neglected for the jet shapes as discussed in Sect. 7.

- To assess the uncertainty associated with the subtraction of background events, the predictions for hadronic decays of the Z^0 and for $\gamma\gamma \to \tau\tau$ reactions are conservatively varied by 10% without contributing significantly to the systematic error. The prediction of the contribution from $\gamma^*\gamma$ events has been scaled up by a factor of two as described above. By comparing the predictions to the data for large $E_{\text{FD}}/E_{\text{BEAM}}$ and M_{J1H2} (see Fig. 2), where this background dominates, we determine that this scaling factor can be varied by no more than about 30% in order to keep a good description of the data. The scaling factor is varied accordingly. The uncertainty from all the background subtraction is typically 2–4%.
- To estimate the systematic error arising from the specific model used for the unfolding, both PYTHIA and PHOJET are used to unfold the data. The estimated uncertainty derived from this study is typically 10%, and up to 20% in some cases for the differential cross-sections, and 1–2% for the jet shapes.
- The absolute energy scale of the ECAL calorimeter is known to about 3% [27] for the range of jet energies in this analysis. To estimate the influence on the observables the energy scale is varied by this amount and the analysis is repeated. The cross-sections change by 5–10% due to this variation. The estimated uncertainty for the jet shapes is about 1%.
- The selection criteria described in Sect. 5 are varied simultaneously both to be more restrictive and to allow more events into the analysis to exclude a strong dependence on the event selection. Selection criteria based on energy measurements are varied by 10% of their central value, which is considered conservative given the
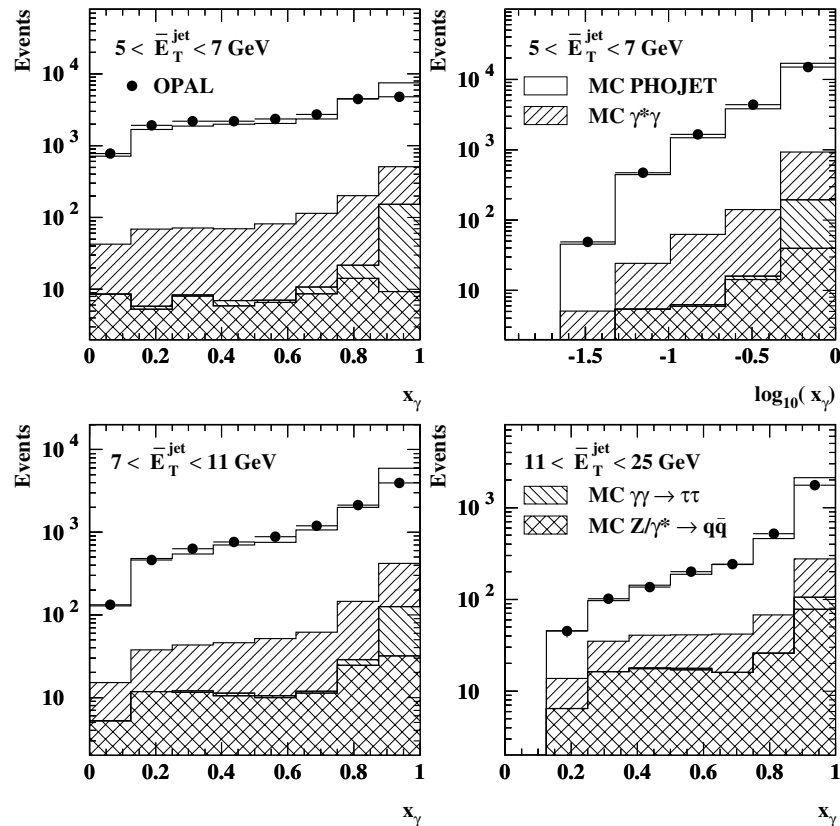
Fig. 5. The uncorrected x_γ distributions in the data compared to the sum of signal and background processes in the simulation. The statistical error is shown where larger than the marker size. The MC simulations used are the same as in Fig. 2

uncertainty in the energy scale and the energy resolution of the calorimeter. The number of tracks required and the maximum net charge of the event are changed by ± 1. The allowed radial distance and z position of the primary vertex are varied by 0.5 cm and 1 cm respectively. The uncertainty on the cross-section derived from all these variations is typically 5–10%, and up to 20% in some cases for the differential cross-section, and about 2–4% for the jet shapes.

The uncertainty on the determination of the integrated luminosity is much less than 1%, and is neglected. For the differential cross-sections the systematic uncertainties evaluated for each bin were averaged with the results from its two neighbours (single neighbour for endpoints) to reduce the effect of bin-to-bin fluctuations.

9 Hadronisation corrections

The differential di-jet cross-sections measured are compared to NLO QCD calculations which predict jet cross-sections for partons, whereas the experimental jet cross-sections are presented for hadrons. Effects due to the modelling of the hadronisation process are not taken into account in the NLO calculation. Because the partons in the MC generators and the partons in the NLO calculations are defined in different ways there is as yet no rigorous

procedure to use the MC generators to correct the data so that they can be compared to the NLO parton level predictions. However, as the MC generators are the only available option so far, they are used to study the approximate size of these hadronisation corrections. For this purpose the prediction of the MC generators at the level of the partonic final state is calculated and divided by the prediction obtained from the hadronic final state. The resulting correction factor is labelled $(1 + \delta_{hadr})$. The partonic final state consists of all partons at the end of the parton shower. The hadronic final state utilises all charged and neutral particles with lifetimes greater than 3×10^{-10} s, which are treated as stable.

Examples of hadronisation corrections estimated by PYTHIA and HERWIG for the observables defined in Sect. 4 are shown in Fig. 6. The numerical values can be found in [28]. In PYTHIA the partonic final state is hadronised according to the string fragmentation model. Since PHOJET uses the same fragmentation model, HERWIG, which uses cluster fragmentation, is used as an alternative model to estimate the effects of hadronisation. In all plots the full x_γ^+-x_γ^--range is considered. The theoretical calculations are corrected bin-by-bin using the mean of the hadronisation corrections estimated using PYTHIA and HERWIG.

Figure 6a shows $(1 + \delta_{hadr})$ as a function of $\bar{E}_T^{jet}$. The correction is less than 10% for $\bar{E}_T^{jet}$ greater than about 10 GeV, but rises to about 25% for PYTHIA and 15% for
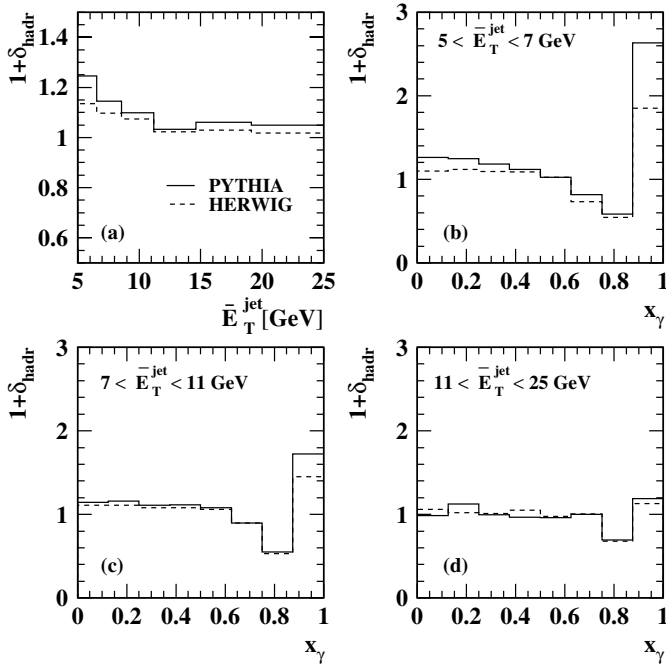
Fig. 6a–d. Hadronisation corrections estimated by PYTHIA and HERWIG for **a** $\bar{E}_T^{jet}$ and **b–d** x_γ for the regions of $\bar{E}_T^{jet}$ given in the figure. In all cases the full x_γ^+-x_γ^--space is considered

Fig. 7a–d. The jet shape, $\Psi(r)$, for the two regions of x_γ^+-x_γ^--space indicated in the figure **a**, and $\Psi(r)$ for $x_\gamma^\pm < 0.75$ compared to the predictions of the LO MC generators PHOJET and PYTHIA **b**. Figures **c** and **d** show the value of $\Psi(r = 0.4)$ as a function of the transverse energy and pseudo-rapidity of the jet respectively, compared to the PYTHIA prediction. The total of statistical and systematic uncertainties added in quadrature is shown where larger than the marker size. The inner error bars show the statistical errors

HERWIG towards small $\bar{E}_T^{jet}$. The corrections for observables involving the jet pseudo-rapidities are dominated by the low $\bar{E}_T^{jet}$ region. They are essentially flat and around 20% for PYTHIA. HERWIG estimates these corrections to be around 10%.

Figure 6b shows $(1 + \delta_{hadr})$ as a function of x_γ for the lowest bin in $\bar{E}_T^{jet}$ defined in Sect. 4. From the figure it is evident that hadronisation causes large corrections for $x_\gamma > 0.75$. The effect is reduced for higher values of $\bar{E}_T^{jet}$, as can be seen in Fig. 6c and d. The large corrections for $x_\gamma > 0.75$ are mainly due to the large influence hadronisation has on the distribution of direct events, which are peaked at $x_\gamma = 1$ for the partonic final state of the LO calculation, but are much more smeared out at the level of stable hadrons (see Fig. 1a–c). The large corrections in this area indicate that the perturbative computation at NLO becomes unreliable as it approaches $x_\gamma = 1$, as discussed in [29, 30]. For a sensible comparison in this region one should therefore consider a more inclusive quantity, such as the sum of the two bins above $x_\gamma = 0.75$, and compare it to the corresponding sum for the data.

10 Results

10.1 Jet structure in di-jet events

In Fig. 7a the jet shape, $\Psi(r)$, is shown for the $k_\perp$ algorithm for both $x_\gamma^\pm > 0.75$ and $x_\gamma^\pm < 0.75$. The first sample is dominated by direct photon-photon interactions and hence by quark-initiated jets. As is demonstrated in the figure, jets in this sample are more collimated than for
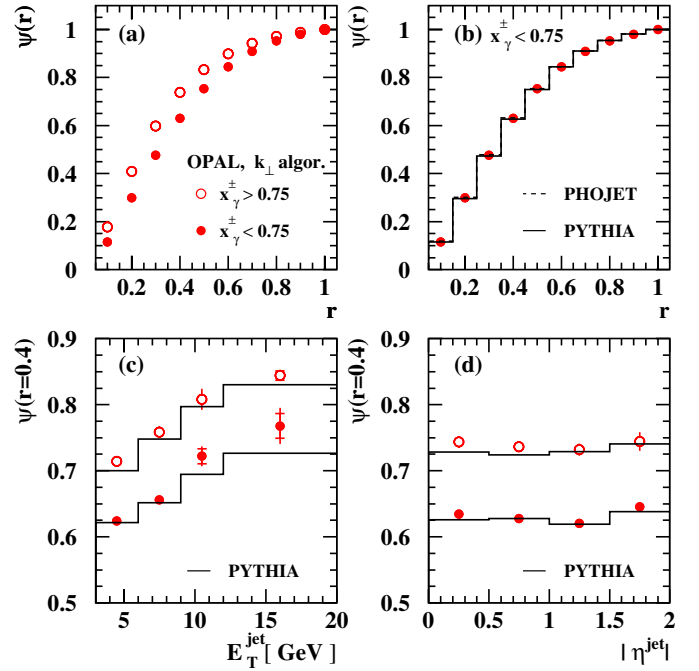
small values of $x_\gamma^\pm$, where the cross-section is dominated by resolved processes and hence has a large contribution from gluon-initiated jets. In both cases the jets become more collimated with increasing transverse energy, as is shown in Fig. 7c. There is no significant dependence on the jet pseudo-rapidity (Fig. 7d). Both PHOJET and PYTHIA give an adequate description of the jet shapes as can be seen in Figs. 7b, c, and d.

Figure 8 compares the shapes of jets defined by the cone algorithm and the $k_\perp$ algorithm, in each case compared to the shape as obtained from PYTHIA. As for the $k_\perp$-jets, the jets defined by the cone algorithm are more collimated in the quark-dominated sample and always become more collimated for increasing transverse energy, while there is no dependence on the jet pseudo-rapidity. The cone-jets are significantly broader than the jets defined by the $k_\perp$ algorithm at low E_T^{jet}. With increasing E_T^{jet}, jets become more collimated and the two jet algorithms give similar results. While the $k_\perp$-jets are well described by PYTHIA and PHOJET, the jet shapes obtained for the cone-jets are somewhat broader than in the data.

10.2 Differential di-jet cross-sections

Only the $k_\perp$ jet algorithm is used for the measurement of the differential di-jet cross-sections. The experimental
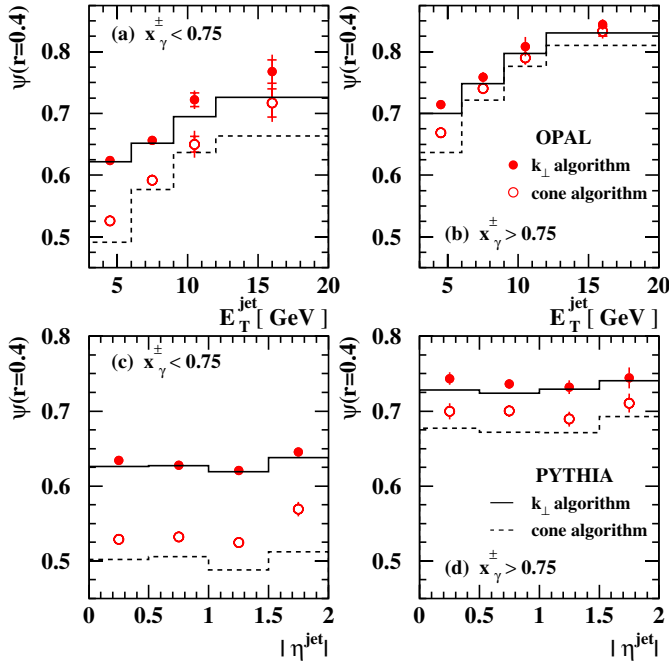
Fig. 8a–d. The value of the jet shape $\Psi(r)$ at $r = 0.4$ as a function of the jet transverse energy for $x_\gamma^\pm < 0.75$ **a** and $x_\gamma^\pm > 0.75$ **b**, and as a function of the jet pseudo-rapidity for $x_\gamma^\pm < 0.75$ **c** and $x_\gamma^\pm > 0.75$ **d**. In each figure the results obtained using the inclusive $k_\perp$ and the cone jet algorithm are shown and compared to the PYTHIA prediction. The total of statistical and systematic uncertainties added in quadrature is shown where larger than the marker size. The inner error bars show the statistical errors

results are compared to a perturbative QCD calculation at NLO [31] which uses the GRV HO parametrisation of the parton distribution functions of the photon [14], and was repeated for the kinematic conditions of the present analysis. The renormalisation and factorisation scales are set to the maximum E_T^{jet} in the event. The calculation was performed in the $\overline{MS}$-scheme with five light flavours and $\Lambda_{QCD}^{(5)} = 130$ MeV. The average of the hadronisation corrections estimated by PYTHIA and HERWIG have been applied to the calculation for this comparison.

Figure 9 and Table 1 show the differential di-jet cross-section as a function of $|\cos \Theta^*|$ for both $x_\gamma^\pm > 0.75$ and $x_\gamma^\pm < 0.75$. The steeper rise with increasing $|\cos \Theta^*|$ from the dominating spin-1 gluon exchange in the second sample is clearly visible (see Sect. 4). PYTHIA using SaS 1D is in good agreement with the measured distributions, with a tendency to be above the data around $|\cos \Theta^*| = 0.5$ for $x_\gamma^\pm > 0.75$. The shaded histogram at the bottom of each plot indicates the MIA contribution to the PYTHIA prediction. The numerical values of this contribution can be found in [28]. The shape of both samples is well described by NLO QCD. For $x_\gamma^\pm < 0.75$ the NLO calculation is 20–30 % below the data. It should be noted that in this region the contribution from the underlying event, not included in the calculation, is expected to be largest. It is interesting to note that the MIA contribution to the cross-section as ob-
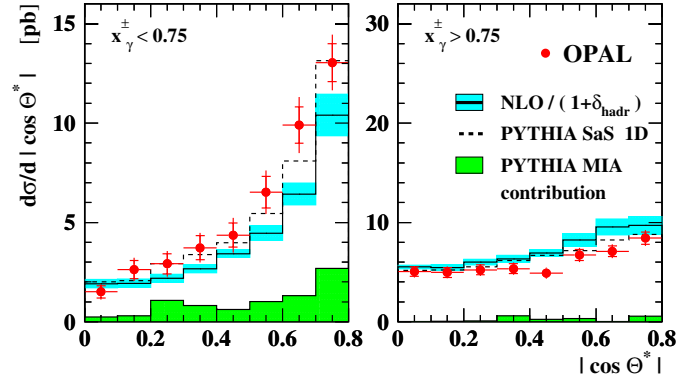

Fig. 9. The di-jet cross-section as a function of $|\cos \Theta^*|$ for the two regions in x_γ^+-x_γ^--space indicated in the figure. The total of statistical and systematic uncertainties added in quadrature is shown where larger than the marker size. The inner error bars show the statistical errors. The numerical values are given in Table 1. The prediction of the LO MC generator PYTHIA using the parton distribution function SaS 1D is compared to the data. The shaded histogram at the bottom of each plot indicates the MIA contribution to the PYTHIA prediction. A perturbative NLO QCD prediction [31] using the GRV HO parton densities is compared to the data after hadronisation corrections have been applied to the calculation. The shaded band indicates the theoretical uncertainty estimated by the quadratic sum of two contributions: variation of the renormalisation scale by factors of 0.5 and 2 and the difference between using HERWIG or PYTHIA in estimating the hadronisation corrections

Table 1. The di-jet cross-section as a function of $|\cos \Theta^*|$ for the two regions in x_γ^+-x_γ^--space indicated in the table. The total uncertainty for each bin is the quadratic sum of the statistical and systematic uncertainty given in the table

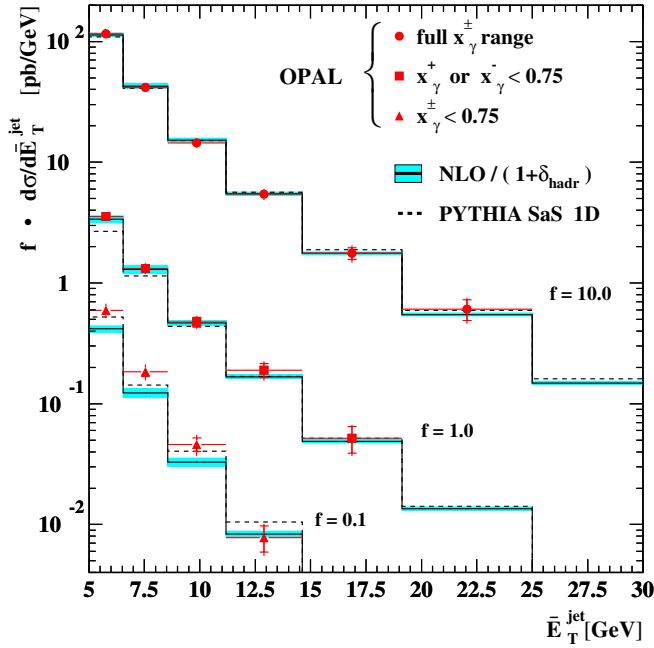| $\|\cos \Theta^*\|$	$d\sigma_{dijet}/d\|\cos \Theta^*\|$ [pb]	$\pm\delta_{stat}$ [pb]	$\pm\delta_{sys}$ [pb]
	$x_\gamma^\pm > 0.75$		
0.0–0.1	5.04	0.49	0.32
0.1–0.2	4.96	0.49	0.34
0.2–0.3	5.22	0.49	0.32
0.3–0.4	5.35	0.48	0.38
0.4–0.5	4.90	0.45	0.32
0.5–0.6	6.73	0.56	0.47
0.6–0.7	7.09	0.54	0.43
0.7–0.8	8.42	0.61	0.51
	$x_\gamma^\pm < 0.75$		
0.0–0.1	1.50	0.31	0.24
0.1–0.2	2.63	0.46	0.36
0.2–0.3	2.91	0.50	0.41
0.3–0.4	3.73	0.62	0.43
0.4–0.5	4.36	0.61	0.62
0.5–0.6	6.52	0.80	0.74
0.6–0.7	9.90	0.92	1.07
0.7–0.8	13.05	0.96	1.02

Fig. 10. The di-jet cross-section as a function of the mean transverse energy $\bar{E}_T^{jet}$ of the di-jet system, for the three regions in x_γ^+-x_γ^--space given in the figure. The factor f is used to separate the three measurements in the figure more clearly. The total of statistical and systematic uncertainties added in quadrature is shown where larger than the marker size. The inner error bars show the statistical errors. The numerical values are given in Table 2. The prediction of the LO program PYTHIA using the parton distribution function SaS 1D is compared to the data. The NLO calculation is the same as in Fig. 9

Table 2. The di-jet cross-section as a function of the mean transverse energy $\bar{E}_T^{jet}$ of the di-jet system, for the three regions in x_γ^+-x_γ^--space indicated in the table

$\bar{E}_T^{jet}$ [GeV]	$d\sigma_{dijet}/d\bar{E}_T^{jet}$ [pb/GeV]	$\pm\delta_{stat}$ [pb/GeV]	$\pm\delta_{sys}$ [pb/GeV]
full x_γ^+ - x_γ^- – range			
5.00–6.54	11.54	0.36	0.59
6.54–8.55	4.16	0.16	0.25
8.55–11.18	1.45	0.07	0.09
11.18–14.62	0.543	0.036	0.044
14.62–19.12	0.176	0.020	0.020
19.12–25.00	0.0607	0.0117	0.0087
x_γ^+ or x_γ^- < 0.75			
5.00–6.54	3.56	0.21	0.22
6.54–8.55	1.32	0.09	0.10
8.55–11.18	0.475	0.045	0.037
11.18–14.62	0.190	0.025	0.024
14.62–19.12	0.0518	0.0127	0.0073
$x_\gamma^\pm$ < 0.75			
5.00–6.54	5.94	0.41	0.66
6.54–8.55	1.84	0.16	0.23
8.55–11.18	0.461	0.060	0.071
11.18–14.62	0.0781	0.0192	0.0130

tained from PYTHIA is similar in size to the discrepancy. For $x_\gamma^\pm > 0.75$ the NLO QCD prediction is about 20 % above the data. While here the contribution from MIA is small, the theoretical prediction becomes unreliable as it approaches $x_\gamma = 1$, as discussed in Sect. 9.

The differential di-jet cross-section as a function of the mean transverse energy $\bar{E}_T^{jet}$ of the di-jet system is shown in Fig. 10 and Table 2. At high $\bar{E}_T^{jet}$ the cross-section is expected to be dominated by direct processes, associated with the region $x_\gamma^\pm > 0.75$. Consequently we observe a significantly softer spectrum for the case $x_\gamma^\pm < 0.75$ than for the full x_γ^+-x_γ^--space. The calculation is in good agreement with the data for the full x_γ^+-x_γ^--range and for x_γ^+ or x_γ^- < 0.75. The cross-section predicted for $x_\gamma^\pm < 0.75$ is again below the measurement. PYTHIA is in good agreement with the measured distributions using the SaS 1D parton densities.

Figure 11 and Tables 3 and 6 show the di-jet cross-section as a function of x_γ and $\log_{10}(x_\gamma)$. The cross-section for the lowest values of $\bar{E}_T^{jet}$ shows the largest fraction of events at $x_\gamma < 0.75$ of the three ranges considered, and is hence most sensitive to gluon-initiated processes. The di-jet cross-section logarithmic in x_γ emphasises the region of

lowest accessible x_γ, which extends down to approximately 0.02.

As $\bar{E}_T^{jet}$ increases, the fraction of events with $x_\gamma > 0.75$ increases. In MC simulations these are predominantly direct events. The sensitivity to the gluon density in the photon is hence expected to decrease with increasing $\bar{E}_T^{jet}$. On the other hand, NLO QCD predictions which use $\bar{E}_T^{jet}$ as the process-relevant scale are expected to become more reliable as this scale increases. It is hence important to provide measurements at both low and high values of $\bar{E}_T^{jet}$, to study all aspects of the theory.

PYTHIA using SaS 1D is in good agreement with the measured distributions, with a tendency to be too low for small values of x_γ. NLO QCD predicts the shape of the cross-sections well for $x_\gamma < 0.75$, but is too low by about 10–20 % especially at low $\bar{E}_T^{jet}$. Again the MIA contribution to the cross-section as obtained from PYTHIA is similar in size to the discrepancy.

The NLO calculation becomes unreliable as it approaches $x_\gamma = 1$ as discussed in Sect. 9. The uncertainty for the data-theory comparison can be reduced [30] by considering the sum of the two bins above $x_\gamma = 0.75$, for which NLO QCD indeed gives an adequate description of the data.

Figure 12 demonstrates the effect of using different parton distribution functions of the photon on the NLO QCD prediction. AFG HO [32] and GS96 HO [33] are used in addition to the default GRV HO. The sensitivity of the cross-section to the different gluon density in each case is clearly visible for the gg-contribution (Fig. 12b), but is
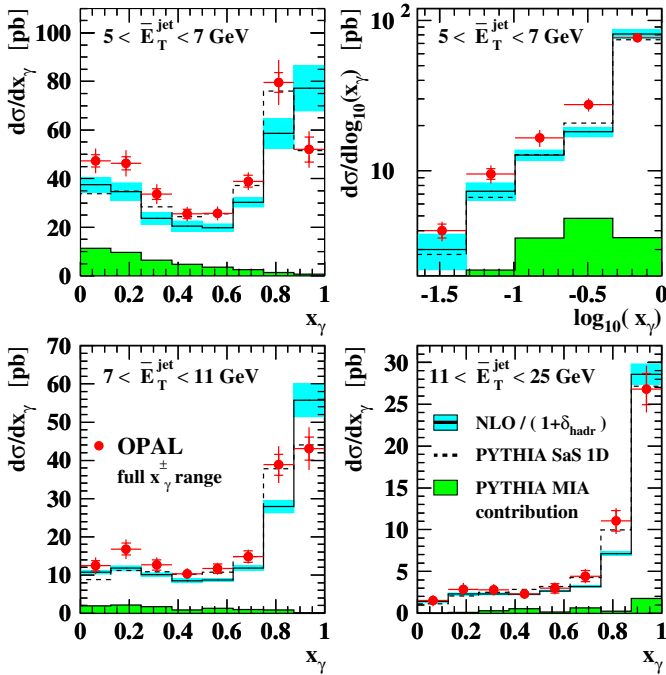
Fig. 11. The di-jet cross-section as a function of x_γ and $\log_{10}(x_\gamma)$ for the regions of the mean transverse energy $\bar{E}_T^{jet}$ of the di-jet system indicated in the figures. The total of statistical and systematic uncertainties added in quadrature is shown where larger than the marker size. The inner error bars show the statistical errors. The numerical values are given in Tables 3 and 6. The prediction of the LO MC generator PYTHIA using the parton distribution function SaS 1D is compared to the data. The shaded histogram at the bottom of each plot indicates the MIA contribution to the PYTHIA prediction. The NLO calculation is the same as in Fig. 9

Table 3. The di-jet cross-section as a function of x_γ for the regions of the mean transverse energy $\bar{E}_T^{jet}$ of the di-jet system and the region in x_γ^+-x_γ^--space indicated in the table

x_γ	$d\sigma_{dijet}/dx_\gamma$ [pb]	$\pm\delta_{stat}$ [pb]	$\pm\delta_{sys}$ [pb]
full x_γ^+ - x_γ^- – range			
5 GeV $< \bar{E}_T^{jet} <$ 7 GeV			
0.000–0.125	47.29	2.51	4.41
0.125–0.250	46.29	2.73	4.69
0.250–0.375	33.66	2.16	3.37
0.375–0.500	25.47	1.93	2.25
0.500–0.625	25.70	1.86	2.16
0.625–0.750	38.91	2.47	2.70
0.750–0.875	79.59	4.07	8.37
0.875–1.000	51.97	5.12	5.49
7 GeV $< \bar{E}_T^{jet} <$ 11 GeV			
0.000–0.125	12.41	1.37	1.70
0.125–0.250	16.78	1.55	2.05
0.250–0.375	12.64	1.34	1.47
0.375–0.500	10.36	1.16	0.86
0.500–0.625	11.67	1.24	0.95
0.625–0.750	14.80	1.53	1.05
0.750–0.875	38.84	2.72	3.99
0.875–1.000	43.07	3.00	4.75
11 GeV $< \bar{E}_T^{jet} <$ 25 GeV			
0.000–0.125	1.51	0.53	0.39
0.125–0.250	2.83	0.52	0.64
0.250–0.375	2.78	0.54	0.43
0.375–0.500	2.30	0.48	0.36
0.500–0.625	2.97	0.57	0.41
0.625–0.750	4.43	0.66	0.55
0.750–0.875	11.04	1.23	0.94
0.875–1.000	26.81	1.85	2.09

less pronounced for the full cross-section as can be seen in Fig. 12a, due to compensating effects from processes involving the quark densities (Figs. 12c and d). A global analysis, beyond the scope of this paper, using for example F_2^γ measurements to constrain simultaneously the quark densities hence promises to yield the highest sensitivity to the gluon density in the photon.

In Fig. 13 (Tables 4 and 6) the same cross-sections as in Fig. 11 are shown for the case x_γ^+ or $x_\gamma^- < 0.75$. Here the cross-section is dominated by interactions where one of the two incident photons is resolved. The multiple parton interactions used in PYTHIA to model an underlying event are much suppressed in this case, and NLO QCD describes both the shape and normalisation of the data well. The opposite effect can be observed in Fig. 14 (Tables 5 and 6), where for the case $x_\gamma^\pm < 0.75$ one expects a large influence of multiple parton interactions, as demonstrated again by the shaded histogram at the bottom of each plot. The cross-sections change by as much as 50% in the low $\bar{E}_T^{jet}$ region, when MIA are switched on. For higher $\bar{E}_T^{jet}$ the influence is not as strong. Even with MIA switched on, PYTHIA using SaS 1D is too low. The deficit visible in the normalisation of the NLO calculation is again of similar size as the MIA contribution to the cross-section obtained from PYTHIA.

Complementary information can be obtained by measuring the angular distributions of the two highest E_T^{jet} jets in di-jet events. The $|\eta^{jet}|$ and $|\Delta\eta^{jet}|$ dependence of the di-jet cross-section is dominated by the low E_T^{jet} events. The cross-sections measured are listed in Tables 7, 8 and 9. In Fig. 15 the di-jet cross-sections as a function of $|\Delta\eta^{jet}|$, $|\eta_{cntr}^{jet}|$ and $|\eta_{fwd}^{jet}|$ are shown for the case x_γ^+ or $x_\gamma^- < 0.75$. Again the multiple parton interactions used in PYTHIA to model an underlying event are much suppressed in this case. PYTHIA using SaS 1D is about 20% too low. The prediction of NLO QCD is in good agreement with the data in both shape and normalisation.

In Fig. 16 the same cross-sections are presented for the case of $x_\gamma^\pm < 0.75$. As expected, the effect of including MIA in PYTHIA is again sizable. When multiple parton interactions are switched on, the prediction obtained from PYTHIA reproduces the data reasonably well. Again the prediction of NLO QCD is too low by about the size of the MIA contribution to the cross-section obtained by PYTHIA.
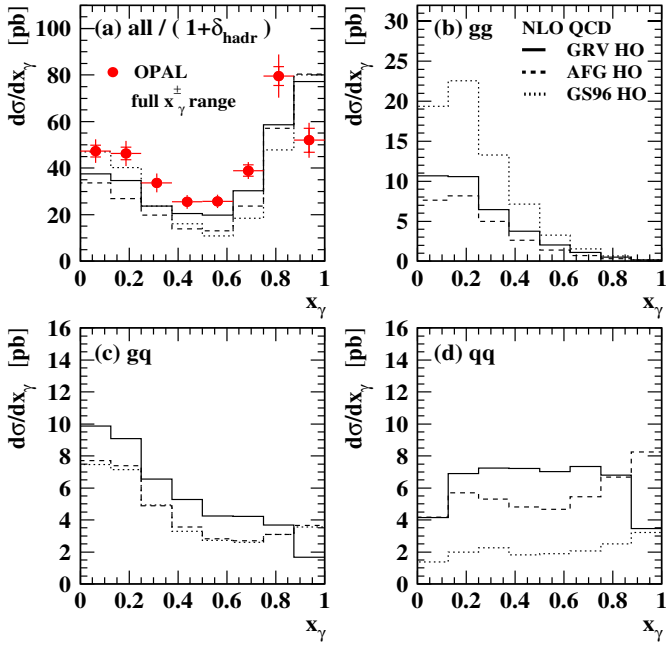
Fig. 12. The prediction of NLO QCD using different parton distributions for the photons. The di-jet cross-section as a function of x_γ for $5\,\text{GeV} < \bar{E}_T^{\text{jet}} < 7\,\text{GeV}$ (upper left plot in Fig. 11) is shown. In **a** the full cross-section is shown after hadronisation corrections have been applied, while **b**, **c** and **d** show the gg, gq and qq contributions to this cross-section without hadronisation corrections. The NLO calculation is the same as in Fig. 9

Table 4. The di-jet cross-section as a function of x_γ for the regions of the mean transverse energy $\bar{E}_T^{\text{jet}}$ of the di-jet system and the region in x_γ^+-x_γ^--space indicated in the table

x_γ	$d\sigma_{\text{dijet}}/dx_\gamma$	$\pm\delta_{\text{stat}}$	$\pm\delta_{\text{sys}}$
	[pb]	[pb]	[pb]
x_γ^+ or $x_\gamma^- < 0.75$			
$5\,\text{GeV} < \bar{E}_T^{\text{jet}} < 7\,\text{GeV}$			
0.000–0.125	12.47	0.96	1.18
0.125–0.250	8.87	0.74	1.16
0.250–0.375	7.00	0.69	0.83
0.375–0.500	5.12	0.58	0.65
0.500–0.625	5.99	0.69	0.56
0.625–0.750	12.36	1.27	0.98
0.750–0.875	38.50	1.92	4.19
0.875–1.000	11.80	1.72	1.30
$7\,\text{GeV} < \bar{E}_T^{\text{jet}} < 11\,\text{GeV}$			
0.000–0.125	5.44	0.73	0.62
0.125–0.250	4.84	0.52	0.48
0.250–0.375	3.45	0.44	0.31
0.375–0.500	2.91	0.41	0.21
0.500–0.625	3.28	0.48	0.25
0.625–0.750	5.38	0.76	0.39
0.750–0.875	15.03	1.17	1.94
0.875–1.000	8.63	1.19	1.31

Table 5. The di-jet cross-section as a function of x_γ for the regions of the mean transverse energy $\bar{E}_T^{\text{jet}}$ of the di-jet system and the region in x_γ^+-x_γ^--space indicated in the table

| x_γ	$d\sigma_{\text{dijet}}/dx_\gamma$	$\pm\delta_{\text{stat}}$	$\pm\delta_{\text{sys}}$
	[pb]	[pb]	[pb]
$x_\gamma^\pm < 0.75$			
$5\,\text{GeV} < \bar{E}_T^{\text{jet}} < 7\,\text{GeV}$			
0.000–0.125	42.37	2.94	4.71
0.125–0.250	37.66	2.44	4.32
0.250–0.375	26.87	1.99	2.66
0.375–0.500	19.63	1.88	1.49
0.500–0.625	17.84	1.55	1.10
0.625–0.750	26.71	3.86	1.73
$7\,\text{GeV} < \bar{E}_T^{\text{jet}} < 11\,\text{GeV}$			
0.000–0.125	8.81	1.08	1.54
0.125–0.250	11.00	1.00	1.72
0.250–0.375	10.30	0.96	1.24
0.375–0.500	8.10	0.81	0.76
0.500–0.625	7.49	0.94	0.64
0.625–0.750	8.51	1.58	0.72

Table 6. The di-jet cross-section as a function of $\log_{10}(x_\gamma)$ for the region of the mean transverse energy $\bar{E}_T^{\text{jet}}$ of the di-jet system and the regions in x_γ^+-x_γ^--space indicated in the table

| $\log_{10}(x_\gamma)$	$d\sigma_{\text{dijet}}/d\log_{10}(x_\gamma)$	$\pm\delta_{\text{stat}}$	$\pm\delta_{\text{sys}}$
	[pb]	[pb]	[pb]
$5\,\text{GeV} < \bar{E}_T^{\text{jet}} < 7\,\text{GeV}$			
full x_γ^+ - x_γ^- – range			
−1.65–−1.32	4.00	0.42	0.42
−1.32–−0.99	9.54	0.76	1.07
−0.99–−0.66	16.55	1.12	1.83
−0.66–−0.33	27.51	1.39	2.35
−0.33–0.00	76.87	1.69	5.05
x_γ^+ or $x_\gamma^- < 0.75$			
−1.65–−1.32	1.29	0.18	0.18
−1.32–−0.99	2.38	0.24	0.32
−0.99–−0.66	3.64	0.30	0.44
−0.66–−0.33	4.87	0.38	0.47
−0.33–0.00	25.87	0.99	2.16
$x_\gamma^\pm < 0.75$			
−1.65–−1.32	3.08	0.44	0.41
−1.32–−0.99	7.81	0.63	1.02
−0.99–−0.66	13.95	0.92	1.55
−0.66–−0.33	19.39	1.13	1.78
−0.33–0.00	18.01	1.53	1.36
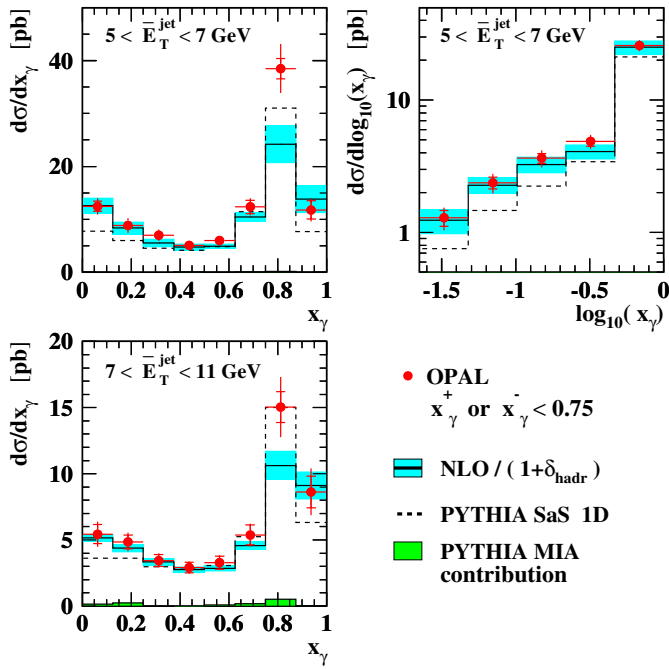
Fig. 13. The di-jet cross-section as a function of x_γ and $\log_{10}(x_\gamma)$ for the regions of the mean transverse energy $\bar{E}_T^{jet}$ of the di-jet system indicated in the figures and for x_γ^+ or $x_\gamma^- < 0.75$. The total of statistical and systematic uncertainties added in quadrature is shown where larger than the marker size. The inner error bars show the statistical errors. The numerical values are given in Tables 4 and 6. The NLO calculation and MC simulation are the same as in Fig. 11
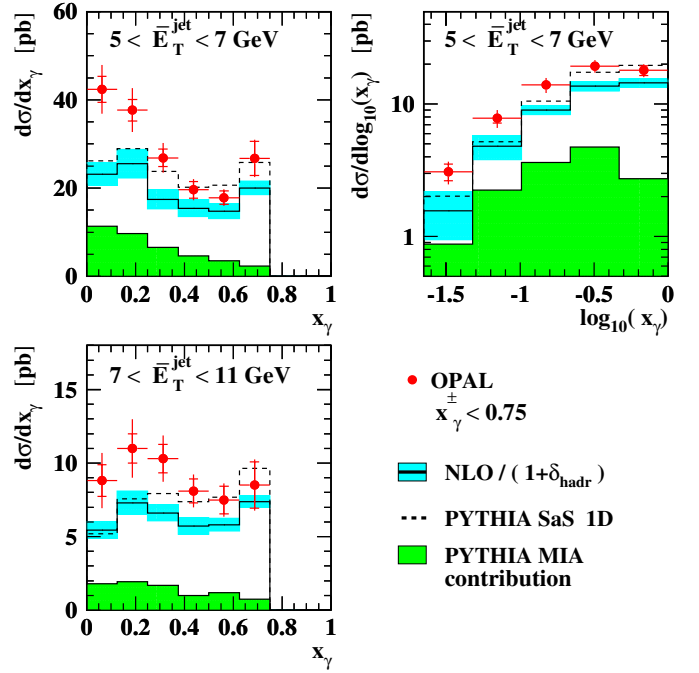
Fig. 14. The di-jet cross-section as a function of x_γ and $\log_{10}(x_\gamma)$ for the regions of the mean transverse energy $\bar{E}_T^{jet}$ of the di-jet system indicated in the figures. For these cross-sections $x_\gamma^\pm < 0.75$ is required. The total of statistical and systematic uncertainties added in quadrature is shown where larger than the marker size. The inner error bars show the statistical errors. The numerical values are given in Tables 5 and 6. The NLO calculation and MC simulation are the same as in Fig. 11

Table 7. The di-jet cross-section as a function of $|\Delta\eta^{jet}|$ for the two leading jets in E_T^{jet}, for the two regions in x_γ^+-x_γ^--space indicated in the table

$|\Delta\eta^{jet}|$	$d\sigma_{dijet}/d|\Delta\eta^{jet}|$	$\pm\delta_{stat}$	$\pm\delta_{sys}$
	[pb]	[pb]	[pb]
x_γ^+ or $x_\gamma^- < 0.75$			
0.0–0.5	6.68	0.27	0.38
0.5–1.0	5.51	0.24	0.31
1.0–1.5	3.98	0.20	0.23
1.5–2.0	2.34	0.15	0.15
2.0–2.5	1.22	0.11	0.11
2.5–3.0	0.631	0.081	0.074
3.0–3.5	0.251	0.056	0.035
$x_\gamma^\pm < 0.75$			
0.0–0.5	7.47	0.36	0.66
0.5–1.0	6.89	0.35	0.60
1.0–1.5	5.42	0.29	0.46
1.5–2.0	3.93	0.24	0.30
2.0–2.5	2.44	0.19	0.30
2.5–3.0	1.43	0.16	0.24
3.0–3.5	0.618	0.124	0.133

Table 8. The di-jet cross-section as a function of $|\eta^{jet}_{cntr}|$ for the two regions in x_γ^+-x_γ^--space indicated in the table

$|\eta^{jet}_{cntr}|$	$d\sigma_{dijet}/d|\eta^{jet}_{cntr}|$	$\pm\delta_{stat}$	$\pm\delta_{sys}$
	[pb]	[pb]	[pb]
x_γ^+ or $x_\gamma^- < 0.75$			
0.00–0.25	11.48	0.50	0.65
0.25–0.50	9.25	0.44	0.55
0.50–0.75	7.19	0.38	0.46
0.75–1.00	5.30	0.32	0.31
1.00–1.25	3.49	0.26	0.23
1.25–1.50	2.60	0.24	0.25
1.50–1.75	1.49	0.21	0.17
$x_\gamma^\pm < 0.75$			
0.00–0.25	14.93	0.67	1.24
0.25–0.50	13.38	0.65	1.17
0.50–0.75	10.83	0.60	0.96
0.75–1.00	7.17	0.47	0.60
1.00–1.25	5.59	0.46	0.54
1.25–1.50	3.20	0.41	0.41
1.50–1.75	2.01	0.41	0.32
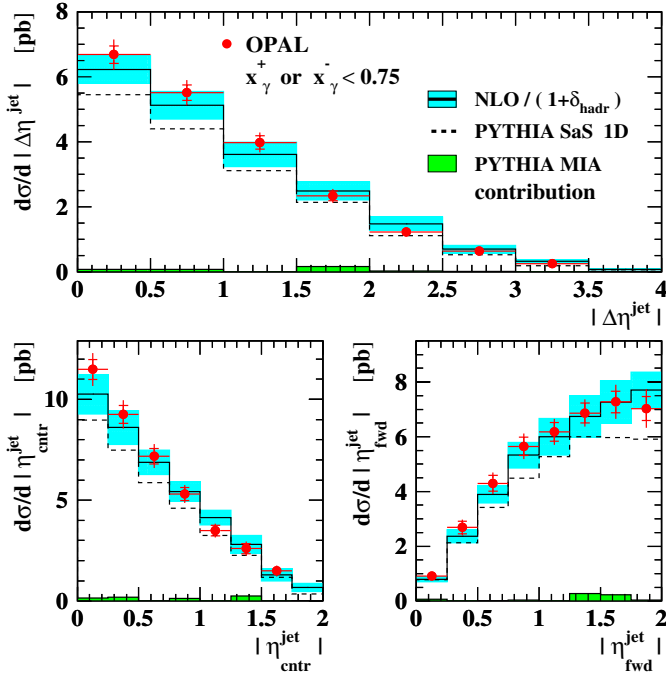
Fig. 15. The di-jet cross-section as a function of $|\Delta\eta^{\mathrm{jet}}|$ for the two leading jets in $E_{\mathrm{T}}^{\mathrm{jet}}$ and separately for the central and the forward jet, for x_γ^+ or $x_\gamma^- < 0.75$. The total of statistical and systematic uncertainties added in quadrature is shown where larger than the marker size. The inner error bars show the statistical errors. The numerical values are given in Tables 7, 8 and 9. The NLO calculation and MC simulation are the same as in Fig. 11

Fig. 16. The di-jet cross-section as a function of $|\Delta\eta^{\mathrm{jet}}|$ for the two leading jets in $E_{\mathrm{T}}^{\mathrm{jet}}$ and separately for the central and the forward jet. For these cross-sections $x_\gamma^\pm < 0.75$ is required. The total of statistical and systematic uncertainties added in quadrature is shown where larger than the marker size. The inner error bars show the statistical errors. The numerical values are given in Tables 7, 8 and 9. The NLO calculation and MC simulation are the same as in Fig. 11

Table 9. The di-jet cross-section as a function of $|\eta_{\mathrm{fwd}}^{\mathrm{jet}}|$ for the two regions in x_γ^+-x_γ^--space indicated in the table

$|\eta_{\mathrm{fwd}}^{\mathrm{jet}}|$	$\mathrm{d}\sigma_{\mathrm{dijet}}/\mathrm{d}|\eta_{\mathrm{fwd}}^{\mathrm{jet}}|$ [pb]	$\pm\delta_{\mathrm{stat}}$ [pb]	$\pm\delta_{\mathrm{sys}}$ [pb]
	x_γ^+ or $x_\gamma^- < 0.75$		
0.00–0.25	0.906	0.137	0.065
0.25–0.50	2.68	0.23	0.18
0.50–0.75	4.30	0.29	0.26
0.75–1.00	5.65	0.33	0.33
1.00–1.25	6.18	0.34	0.33
1.25–1.50	6.86	0.36	0.34
1.50–1.75	7.27	0.40	0.48
1.75–2.00	7.03	0.44	0.55
	$x_\gamma^\pm < 0.75$		
0.00–0.25	1.03	0.17	0.16
0.25–0.50	4.11	0.38	0.54
0.50–0.75	5.64	0.40	0.60
0.75–1.00	6.71	0.41	0.51
1.00–1.25	8.40	0.47	0.74
1.25–1.50	10.72	0.62	0.94
1.50–1.75	11.30	0.68	1.18
1.75–2.00	9.86	0.72	0.96

11 Conclusions

We have studied di-jet production in photon-photon interactions with the OPAL detector at e^+e^- centre-of-mass energies $\sqrt{s_{ee}}$ from 189 to 209 GeV with an integrated luminosity of 593 pb^{-1}. The data are combined into one sample with a luminosity weighted average centre-of-mass energy of approximately $\sqrt{s_{ee}} = 198.5$ GeV. Jets are reconstructed using an inclusive $k_\perp$-clustering algorithm for the measurement of differential di-jet cross-sections, and using both the inclusive $k_\perp$ and a cone algorithm for the study of jet structure.

Jet shapes, $\Psi(r)$, have been studied in two separate samples: $x_\gamma^\pm > 0.75$, which is dominated by direct processes and hence by quark-initiated jets, and $x_\gamma^\pm < 0.75$, dominated by resolved events and therefore by gluon-initiated jets. As expected from QCD the jets in the first sample are significantly more collimated than for $x_\gamma^\pm < 0.75$. Jets in both samples become more collimated with increasing transverse energy, but show no significant dependence on the jet pseudo-rapidity. Jets defined by the cone algorithm are substantially broader than those defined by the $k_\perp$ algorithm at low $E_{\mathrm{T}}^{\mathrm{jet}}$. However the difference decreases with increasing $E_{\mathrm{T}}^{\mathrm{jet}}$. The shape of $k_\perp$-jets is well described by PYTHIA and PHOJET. The jet shapes obtained for the cone-jets are somewhat broader in PYTHIA and PHOJET than in the data.

Inclusive differential di-jet cross-sections have been measured as a function of $|\cos \Theta^*|$, $\bar{E}_T^{jet}$, $|\eta^{jet}|$ and $|\Delta\eta^{jet}|$ and, for the first time, as a function of x_γ in several bins of $\bar{E}_T^{jet}$. Different regions of the x_γ^+-x_γ^--space are explored to separate experimentally direct from resolved interactions and to study and control the influence of an underlying event. By measuring the cross-sections for events in which either x_γ^+ or x_γ^- is smaller than 0.75 we have isolated a region of phase space in which resolved photon processes dominate, and which at the same time is much less sensitive to multiple parton interactions. By performing the measurement also for $x_\gamma^\pm < 0.75$, observables are made available which are sensitive to the amount of multiple parton interactions added in the prediction, and which can be used to study these effects in detail.

A strong rise with increasing $|\cos \Theta^*|$ is observed for the differential di-jet cross-section for $x_\gamma^\pm < 0.75$, as expected from QCD for a sample with a significant contribution from spin-1 gluon exchange. The flatter distribution for direct events is also in good agreement with the QCD calculation.

The differential di-jet cross-sections as a function of $\bar{E}_T^{jet}$, $|\eta^{jet}|$, $|\Delta\eta^{jet}|$ and x_γ are in good agreement with the next-to-leading order perturbative QCD calculation except for x_γ approaching unity, where the calculation becomes unreliable [29,30], and in the double resolved enhanced region of $x_\gamma^\pm < 0.75$, where the calculation is too low. As this calculation does not include a model for the underlying event that is expected to be largest in the latter region, it is interesting to note that the discrepancy here is of similar size to the contribution of multiple parton interactions to the PYTHIA prediction. The sensitivity of the results presented to the gluon density in the photon is clearly visible in NLO QCD predictions using different parton distribution functions, but is compensated to some extent by anti-correlated differences in the respective quark-densities. A global analysis using additional data sets to simultaneously constrain the quark densities hence promises to yield the highest sensitivity to the gluon density in the photon.

The measurements carried out for events in which only either x_γ^+ or x_γ^- is smaller than 0.75 are a unique data set. While this region is almost insensitive to multiple parton interactions, the fraction of events at small x_γ is still sizable, which indicates a significant contribution of resolved processes and hence a good sensitivity to the hadronic structure of the photon. The good agreement of data and theory in this region in particular confirms that perturbative QCD in next-to-leading order is able to describe correctly the inclusive production of di-jets in photon-photon collisions in regions where the theory is expected to be reliable.

References

1. AMY Collaboration, B.J. Kim et al., Phys. Lett. B **325**, 248 (1994)
2. TOPAZ Collaboration, H. Hayashii et al., Proceedings of Photon '95, Sheffield, UK, 8–13 April 1995, edited by D.J. Miller, S.L. Cartwright and V. Khoze, World Scientific (Singapore) 1995, p133; TOPAZ Collaboration, H. Hayashii et al., Phys. Lett. B **314**, 149 (1993)
3. OPAL Collaboration, K. Ackerstaff et al., Z. Phys. C **73**, 433 (1997)
4. OPAL Collaboration, G. Abbiendi et al., Eur. Phys. J. C **10**, 547 (1999)
5. S. Catani, Yu.L. Dokshitzer, M.H. Seymour and B.R. Webber, Nucl. Phys. B **406**, 187 (1993); S.D. Ellis, D.E. Soper, Phys. Rev. D **48**, 3160 (1993)
6. OPAL Collaboration, R. Akers et al., Z. Phys. C **63**, 197 (1994)
7. M. Wobisch and T. Wengler, hep-ph/9907280; M.H. Seymour, hep-ph/9707349; S.D. Ellis, Z. Kunszt and D.E. Soper, Phys. Rev. Lett. **69**, 3615 (1992)
8. C.H. Llewellyn Smith, Phys. Lett. B **79**, 83 (1978)
9. OPAL Collaboration, K. Ahmet et al., Nucl. Instrum. Methods A **305**, 275 (1991); S. Anderson et al., Nucl. Instrum. Methods A **403**, 326 (1998); OPAL Collaboration, G. Abbiendi et al., Eur. Phys. J. C **14**, 373 (2000)
10. T. Sjöstrand, Comp. Phys. Comm. **82**, 74 (1994); T. Sjöstrand, LUND University Report, LU-TP-95-20 (1995).
11. G.A. Schuler and T. Sjöstrand, Z. Phys. C **73**, 677 (1997); G.A. Schuler and T. Sjöstrand, Nucl. Phys. B **407**, 539 (1993)
12. R. Engel, Z. Phys. C **66**, 203 (1995); R. Engel and J. Ranft, Phys. Rev. D **54**, 4244 (1996)
13. G.A. Schuler and T. Sjöstrand, Z. Phys. C **68**, 607 (1995)
14. M. Glück, E. Reya and A. Vogt, Phys. Rev. D **45**, 3986 (1992); M. Glück, E. Reya and A. Vogt, Phys. Rev. D **46**, 1973 (1992)
15. H1 Collaboration, C. Adloff et al., Eur. Phys. J. C **1**, 97 (1998); ZEUS Collaboration, J. Breitweg et al., Eur. Phys. J. C **1**, 109 (1998); ZEUS Collaboration, J. Breitweg et al., Eur. Phys. J. C **4**, 591 (1998); ZEUS Collaboration, J. Breitweg et al., Eur. Phys. J. C **11**, 35 (1999)
16. F.A. Berends, P.H. Daverveldt and R. Kleiss, Nucl. Phys. B **253**, 421 (1985); F.A. Berends, P.H. Daverveldt and R. Kleiss, Comp. Phys. Comm. **40**, 271 (1986), 285 and 309.

17. G. Marchesini et al., Comp. Phys. Comm. **67**, 465 (1992); G. Corcella et al., JHEP **0101**, 010 (2001)
18. J. Allison et al., Nucl. Instrum. Methods A **317**, 47 (1992)
19. L. Lönnblad and M. Seymour (convenors), $\gamma\gamma$ Event Generators, in "Physics at LEP2", CERN 96-01, eds. G. Altarelli, T. Sjöstrand and F. Zwirner, Vol. **2**, 187 (1996)
20. for example: H. Kolanoski, Two-Photon Physics at e^+e^- Storage Rings, Springer-Verlag (1984); B.L. Combridge, J. Kripfganz and J. Ranft, Phys. Lett. B **70**, 234 (1977); D.W. Duke and J.F. Owens, Phys. Rev. D **26**, 1600 (1982)
21. M. Klasen and G. Kramer, Phys. Lett. B **366**, 385 (1996); S. Frixione and G. Ridolfi, Nucl. Phys. B **507**, 315 (1997)
22. H1 Collaboration, C. Adloff et al., Eur. Phys. J. C **1**, 97 (1998)
23. M.H. Seymour, Nucl. Phys. B **513**, 269 (1998)
24. A.M. Rooke (for the OPAL collaboration), Proceedings of Photon '97, Egmond aan Zee, The Netherlands, 10–18 May 1997, edited by A.Buijs and F.C.Erné, World Scientific (Singapore) 1997, p465; A.M. Rooke, University of London, PhD Thesis, September 1998.
25. H1 Collaboration, S. Aid et al., Z. Phys. C **70**, 17 (1996)
26. A. Höcker, V. Kartvelishvili, Nucl. Instrum. Methods A **372**, 469 (1996)
27. OPAL Collaboration, G. Abbiendi et al., Eur. Phys. J. C **14**, 199 (2000)
28. HEPDATA: The Durham RAL Databases, Durham Database Group, at Durham University(UK), http://www-spires.dur.ac.uk/HEPDATA.
29. M. Klasen, Rev. Mod. Phys. **74**, 1221 (2002)
30. L. Bertora and S. Frixione, Proceedings of Photon '03, Frascati, Italy, 7–11 April 2003, edited by F. Anulli, S. Braccini and G. Pancheri, to be published in Nucl. Phys. B; hep-ph/0306167.
31. M. Klasen, T. Kleinwort and G. Kramer, Eur. Phys. J. Direct C **1**, 1 (1998); B. Pötter, Eur. Phys. J. Direct C **5**, 1 (1999)
32. P. Aurenche, J.P. Guillet and M. Fontannaz, Z. Phys. C **64**, 621 (1994)
33. L.E. Gordon and J.K. Storrow, Nucl. Phys. B **489**, 405 (1997)